



# Regulation of electronic structure in medium-entropy metal sulfides nanoparticles as highly efficient bifunctional electrocatalysts for zinc-air battery

Hao Wu<sup>a,1</sup>, Zexu Li<sup>b,1</sup>, Zhichao Wang<sup>a,1</sup>, Yujie Ma<sup>a</sup>, Sirui Huang<sup>c</sup>, Fan Ding<sup>d</sup>, Fengqi Li<sup>a</sup>, Qingxi Zhai<sup>a</sup>, Yilun Ren<sup>a</sup>, Xiaowen Zheng<sup>a</sup>, Yurong Yang<sup>a</sup>, Shaochun Tang<sup>a</sup>, Yu Deng<sup>a,\*</sup>, Xiangkang Meng<sup>a,\*</sup>

<sup>a</sup> National Laboratory of Solid State Microstructures, Collaborative Innovation Center of Advanced Microstructures, College of Engineering and Applied Sciences, Nanjing University, Nanjing 210093, PR China

<sup>b</sup> College of Chemical Engineering, Beijing University of Chemical Technology, Beijing 100029, PR China

<sup>c</sup> College of Materials Science and Engineering, Nanjing University of Science and Technology, Nanjing 210094, PR China

<sup>d</sup> Department of Computer Science, Purdue University, West Lafayette, IN 47907, USA

## ARTICLE INFO

### Keywords:

Electronic structure  
Medium-entropy metal sulfides nanoparticles  
Oxygen evolution reaction  
Oxygen reduction reaction  
Zinc-air batteries

## ABSTRACT

Medium/high-entropy materials have attracted more and more attention in catalytic field in view of their unique properties, yet the related catalytic mechanisms remain ambiguous. Herein, we demonstrate a two-step method for the preparations of medium-entropy metal sulfides (MESs) nanoparticles through the sulfuration of metal-organic frameworks (MOFs) precursors. Compared with the MOF precursor, MES has better electrocatalytic performance in oxygen evolution and reduction reactions (OER/ORR). Electron energy loss spectroscopy (EELS) and X-ray photoelectron spectroscopy (XPS) characterization indicate that the sulfidation can lead metallic ions to possessing higher valence states. Furthermore, the regulation of electronic structure are further proved by density functional theory (DFT) calculations. Rechargeable zinc-air batteries assembled with the  $\text{Fe}_{1.2}(\text{CoNi})_{1.8}\text{S}_6$  MES nanoparticles catalyst superior performances outperforming the commercial catalyst ( $\text{Pt/C}+\text{RuO}_2$ ). The reported two-step method of fabrication strategy for preparing medium-entropy metal sulfides may further contribute to fundamental research into and industrial applications of medium-entropy materials in the rechargeable zinc-air batteries.

## 1. Introduction

Rechargeable metal-air batteries have become a kind of promising renewable energy system in electronic products because of their high theoretical energy density, excellent cycle stability and high security [1–3]. Among them, zinc-air batteries (ZABs) have attracted more attention due to the high theoretical specific energy density (1086 Wh/kg, including oxygen), outstanding safety and nature abundance [4]. For instance, ZABs own better cycle stability compared with aluminum-air battery [5], as well as lower cost and higher security compared with lithium-air battery [6]. However, the application of industrial zinc-air batteries is currently restricted by the sluggish kinetics of the oxygen evolution and reduction reactions (OER/ORR) due to the

large-scale molecular rearrangements to form  $\text{O}=\text{O}$  bonds and four-electron transfer pathways [7–10]. Efficient noble-metal catalysts (e.g.,  $\text{Pt/C}$ ,  $\text{RuO}_2$ ,  $\text{IrO}_2$ ) must be used to enhance reaction rate of OER and ORR, but their high cost have kept them from large-scale commercialization of zinc-air batteries [11–14]. To sum up, the development of inexpensive high-activity catalysts is a choke point in the current field of zinc-air batteries.

Transition metal elements such as Fe, Co, and Ni have the advantages of low cost, low toxicity, and high theoretical catalytic activity [15,16]. Hence, these transition metal materials have been widely studied as OER/ORR electrocatalysts to boost the overall performance of metal-air battery [17–19]. Although Fe, Co or Ni unary metallic catalyst processes certain catalytic performance, the catalytic efficiency needs to be further

\* Corresponding authors.

E-mail addresses: [dengyu@nju.edu.cn](mailto:dengyu@nju.edu.cn) (Y. Deng), [mengxk@nju.edu.cn](mailto:mengxk@nju.edu.cn) (X. Meng).

<sup>1</sup> There authors contributed equally to this work.

enhanced due to the lack of synergistic advantages [20–23]. Zhang et al. synthesize a single-phase bimetallic sulfide ((Ni,Co)S<sub>2</sub>) as an efficient bifunctional electrocatalyst for both OER and ORR [21], where the results show that unique morphology optimizes the active sites and accelerates charge transfer, leading to the enhancement of the catalytic activity. Compared with unary metallic sulfide catalyst (NiS<sub>2</sub>, CoS<sub>2</sub>), the bimetallic sulfide catalyst ((Ni,Co)S<sub>2</sub>) exhibited superior OER/ORR activity (overpotential ( $\eta$ ) = 270 mV at 10 mA cm<sup>-2</sup>, Tafel slope is 88 mV dec<sup>-1</sup> and half-wave potential ( $E_{1/2}$ ) = 0.71 V). In addition, (Ni,Co)S<sub>2</sub> can be used as air electrode in zinc-air batteries, which displays an enhanced charge-discharge property, large specific capacity and outstanding cycling stability. Theoretically, the catalytic activity of ternary and multi-metals is greatly boosted due to the synergistic effect yet lacking relevant reports. The multiplicity synergy is partially inhibited due to the reduction of carrier mobility caused by the formation of complex structural compounds [24].

High-entropy materials (HEMs) with particular microstructure and unparalleled physical and chemical properties have aroused great interest in many different research fields [25–28]. Recently, Ting et al. reported a novel high-entropy material (HEM), namely, high-entropy glyceride (HEG) without precious metals. The HEG is composed of five different metals Fe, Ni, Co, Cr and Mn [27]. Compared to binary, ternary and quaternary metallic glycerate, HEGs containing simple structure exhibit excellent oxygen evolution reaction (OER) activity in 1 M KOH electrolytes, with overpotentials of 229 and 278 mV at 10 mA cm<sup>-2</sup> and 100 mA cm<sup>-2</sup>, respectively. HEGs also present superb stability and durability in alkaline electrolytes. The results indicate the importance of synergistic effects, which provide additional motivation for regulating the electronic structure and coordination environment. Therefore, it is possible to achieve multiple synergistic effects through high entropy structures, which enhance excellent catalytic properties substantially [27,28]. Nevertheless, the high price of raw materials and the difficulty in recycling limit the potential applications of high-entropy materials [29,30]. Under such circumstances, lower price medium-entropy materials (MEMs) have become a new research hotspot because of the superior performance over HEMs [31–33]. For instance, the MEAs and HEAs were used as efficient OER catalysts in alkaline media [32]. The results show that Fe<sub>60</sub>(CoNi)<sub>30</sub>Cr<sub>10</sub> MEA has better OER performance than CoCrFeMnNi high entropy alloy. Compared with bare Fe<sub>60</sub>(CoNi)<sub>30</sub>Cr<sub>10</sub>, the overpotential of the Fe<sub>60</sub>(CoNi)<sub>30</sub>Cr<sub>10</sub> after anodizing decreases significantly. This study proves that the performance of medium-entropy materials may be superior to high-entropy materials in the field of electrocatalysis. Meanwhile, the mixed entropy of MEMs is close to that of conventional materials due to the relatively small number of main elements, which has better prospects in catalytic applications compared with HEMs.

Among recent reports, most nanoscale medium/high entropy materials as electrocatalysts were prepared under complex technological conditions [26,28,34,35]. For example, nanostructured medium/high entropy alloys were prepared via carbonthermal shock method [34]. The above method requires specially made equipment (rapid heating/cooling, 10<sup>5</sup> K/s), high temperature (~2000 K) and conductive substrate (carbon nanofibers). Derivatives were prepared using MOF as precursor, which has been proved to be an effective method for the preparation of medium/high entropy materials [36,37]. It is found that the MOFs-derived materials showed high specific area and excellent electrocatalytic performance with the incorporation of non-metallic elements (C, N, O, S, etc.) [36–39]. Among most of the preparation process, MOFs-derived materials are prepared by pyrolysis. However, it is worth noting that the pyrolysis method often results in the loss of organic ligands and metal agglomeration, and further decreases the number of active sites, or even worse, destroys the structure completely [40]. Therefore, it remains a challenge to develop a simple process to prepare medium-entropy catalysts without pyrolysis. Furthermore, it is significant to regulate the electronic structure of metal atoms in MOFs via preparing MOFs-derived materials.

Herein, we prepared a series medium-entropy metal sulfides Fe<sub>1.2</sub>(CoNi)<sub>1.8</sub>S<sub>x</sub> nanoparticles using a simple two-step method. The MOF precursors were synthesized by ultrasound method and medium-entropy metal sulfides were prepared by solvothermal method. The new design thought was proposed to improve OER/ORR performances via regulating the electronic structure of metal sites in MOFs. Compared with MOF precursors, medium-entropy metal sulfides exhibit excellent OER/ORR activity in alkaline medium. The air electrode made of Fe<sub>1.2</sub>(CoNi)<sub>1.8</sub>S<sub>6</sub> nanoparticles showed excellent performance in rechargeable zinc-air batteries. Moreover, analysis of the change of electronic structure performed by EELS, XPS and DFT calculations systematically reveals the catalytic mechanism of medium-entropy metal sulfides.

## 2. Experimental

### 2.1. Electrocatalyst synthesis

All the chemicals were obtained commercially and employed without further purification, which are presented in Text S1 in the Supporting Information (SI). The details procedures of electrocatalyst preparation are presented in Text S2. And the characterization methods are described in Text S3.

### 2.2. Electrochemical performance evaluation

Electrochemical tests were operated on a three-electrode in electrochemical workstation (CHI 760E) at room temperature. Catalysts, platinum sheet and Ag/AgCl (KCl saturated) were served as working electrode, counter electrode as well as reference electrode, respectively. Details of the OER and ORR experiments are presented in Text S4. The fabrication and testing of rechargeable Zn-air battery are detailed in Text S5.

### 2.3. Computational methods

Density functional theory (DFT) calculations were provided for theoretical proof using Vienna Ab initio Simulation Package (VASP) [41, 42]. Exchange and correlation interactions are explained by generalized gradient approximation (GGA) of Perdew-Burke-Ernzerhof (PBE) in all computations [43]. More details are provided in Text S6.

## 3. Results and discussion

### 3.1. Characterization

A schematic of Fe<sub>x</sub>(CoNi)<sub>3-x</sub>-MOFs and Fe<sub>1.2</sub>(CoNi)<sub>1.8</sub>S<sub>x</sub> medium-entropy metal sulfides (MESs) is outlined in Fig. 1a. Briefly, ternary Fe<sub>x</sub>(CoNi)<sub>3-x</sub>-MOFs are converted to medium-entropy metal sulfides nanoparticles by sulfuration. The X-ray diffraction (XRD) peaks at 8.9°, 15.6° and 17.8° (Fig. S1) can be attributed to the (200), (001) and (201) crystallographic planes of MOF precursors, respectively, which are well accorded with that of previously reported NiFe-BDC [44]. With the value of x in Fe<sub>x</sub>(CoNi)<sub>3-x</sub>-MOFs increasing from 0.6 to 1.4, the main peak around 8.9° widens gradually accompanied by shifting to the right, which suggested that the amorphous degree of the MOF precursors increases. Fe<sub>1.2</sub>(CoNi)<sub>1.8</sub>-MOF precursors were vulcanized in different degrees to obtain Fe<sub>1.2</sub>(CoNi)<sub>1.8</sub>S<sub>x</sub> MESs, and the relevant XRD pattern is shown in Fig. S2. Major diffraction peaks in XRD pattern of Fe<sub>1.2</sub>(CoNi)<sub>1.8</sub>S<sub>x</sub> MESs could be well indexed to (−212), (−143) and (−127) planes of structure, which conform to similar crystal structure of sulfide (PDF #51–0718). Further, with the increase of sulfurization, the crystal structure of Fe<sub>1.2</sub>(CoNi)<sub>1.8</sub>S<sub>x</sub> MESs changes from (−143) preferred orientation to (−212) preferred orientation. Different crystal plane orientations may affect the oxygen evolution reaction (OER) activity of samples by regulating the catalytic active sites and surface atomic

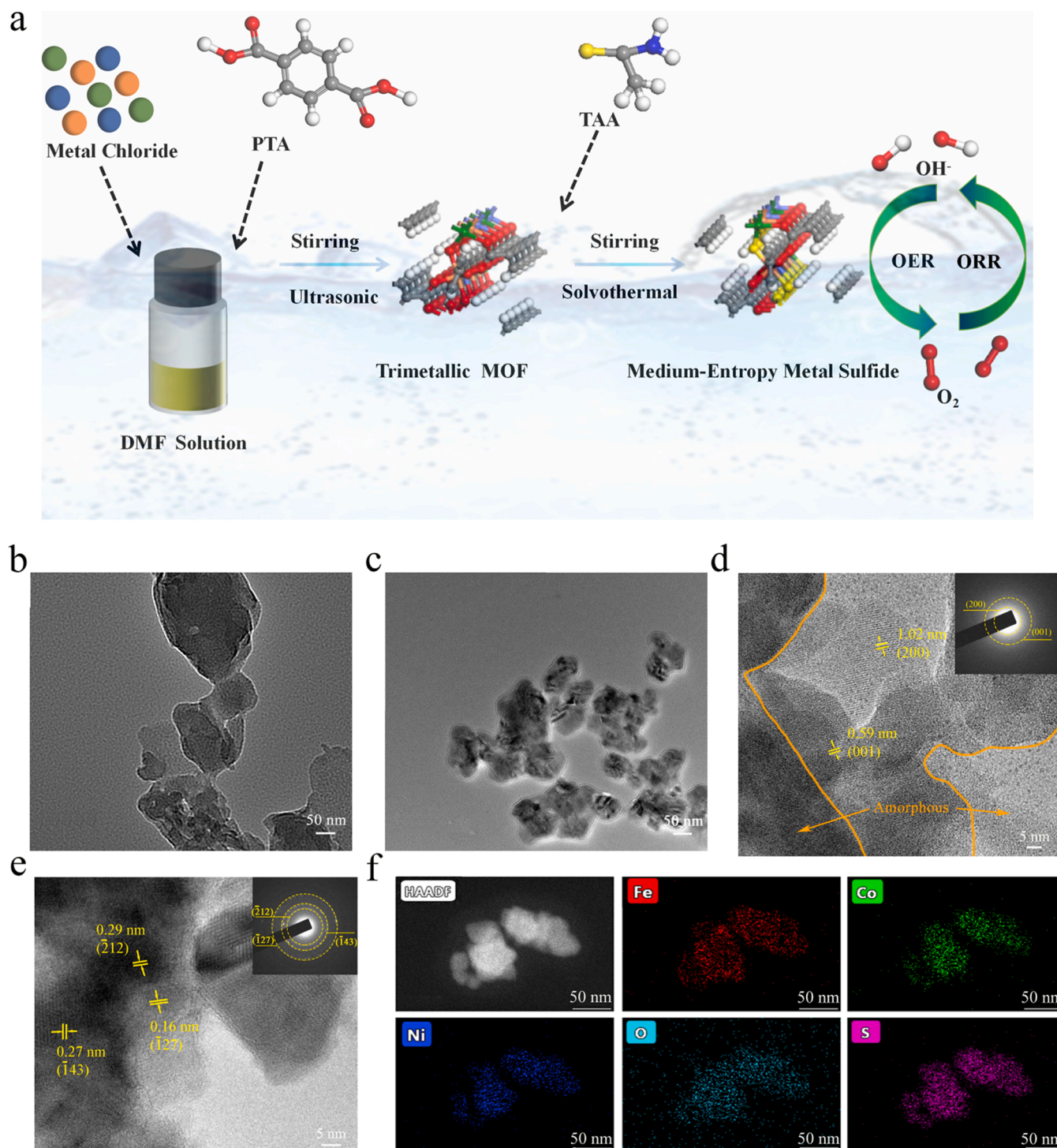


**Fig. 1.** (a) Schematic illustration of  $\text{Fe}_x(\text{CoNi})_{3-x}\text{-MOFs}$  and  $\text{Fe}_{1.2}(\text{CoNi})_{1.8}\text{S}_x$  MESs. TEM images of (b)  $\text{Fe}_{1.2}(\text{CoNi})_{1.8}\text{-MOF}$  and (c)  $\text{Fe}_{1.2}(\text{CoNi})_{1.8}\text{S}_6$  MES. HRTEM images of (d)  $\text{Fe}_{1.2}(\text{CoNi})_{1.8}\text{-MOF}$  and (e)  $\text{Fe}_{1.2}(\text{CoNi})_{1.8}\text{S}_6$  MES. Inset of (d) and (e) are the corresponding SAED patterns. (f) HAADF-STEM image and corresponding elemental mapping of  $\text{Fe}_{1.2}(\text{CoNi})_{1.8}\text{S}_6$  MES.

configurations [45].

Transmission electron microscopy (TEM) is used to observe the morphology of  $\text{Fe}_x(\text{CoNi})_{3-x}\text{-MOFs}$  and  $\text{Fe}_{1.2}(\text{CoNi})_{1.8}\text{S}_x$  MESs, respectively (Fig. S3,S4). With the increase of  $x$ , there is no obvious change in the morphology of  $\text{Fe}_x(\text{CoNi})_{3-x}\text{-MOFs}$ , except that the morphology tends to be more and more amorphous. After sulfuration, the MOF precursors are formed to sulfide particles. The particles size of  $\text{Fe}_{1.2}(\text{CoNi})_{1.8}\text{S}_x$  MESs decreases obviously with the increase of  $x$ , but the agglomeration becomes more obvious. To further compare the change of

sample morphology before and after sulfuration intuitively, spherical aberration-corrected transmission electron microscopy image presents that the obtained  $\text{Fe}_{1.2}(\text{CoNi})_{1.8}\text{-MOF}$  precursor has a morphology of irregular agglomeration (Fig. 1b). After proper sulfuration, obvious variations in different size and dispersion are exhibited (Fig. 1c). The slow diffusion rate of multi-principal elements in the medium-entropy system is an important factor limiting the coordinated diffusion, which leads the material to becomes saturated fleetly, namely, ultrafine-grained nano-scale particles are easily formed. The dispersed



nanoparticles can improve the OER/ORR performance of the samples.

Furthermore, the  $N_2$  adsorption-desorption isotherm estimates the Brunauer Emmett Teller (BET) surface area and pore size distribution display on the as-synthesized samples of  $Fe_x(CoNi)_{3-x}$ -MOFs and  $Fe_{1.2}(CoNi)_{1.8}S_6$  MESs (Fig. S5,S6).  $Fe_{1.2}(CoNi)_{1.8}$ -MOF and  $Fe_{1.2}(CoNi)_{1.8}S_6$  MES has the largest surface area in  $Fe_x(CoNi)_{3-x}$ -MOFs and  $Fe_{1.2}(CoNi)_{1.8}S_6$  MESs, respectively. The BET and Langmuir surface area of  $Fe_{1.2}(CoNi)_{1.8}$ -MOF was evaluated to be around  $39.3\text{ m}^2/\text{g}$  and  $72.2\text{ m}^2/\text{g}$ . The pore volume and average pore size was estimated to be  $0.343\text{ cm}^3/\text{g}$  and  $30.8\text{ nm}$ , respectively. Besides, for  $Fe_{1.2}(CoNi)_{1.8}S_6$  MES, BET and Langmuir surface area is  $49.4\text{ m}^2/\text{g}$  and  $90.4\text{ m}^2/\text{g}$ , while the pore volume and average pore size are determined to be  $0.421\text{ cm}^3/\text{g}$  and  $30.0\text{ nm}$ , respectively. The larger the pore volume and the smaller the average pore size lead to the larger specific surface area [46]. Therefore, nano-sized  $Fe_{1.2}(CoNi)_{1.8}S_6$  MES has larger specific surface area than micron-sized MOF precursor. As can be seen in Fig. S5d,S6b, the distribution of pore size of  $Fe_{1.2}(CoNi)_{1.8}S_6$  MES is more even than that of  $Fe_{1.2}(CoNi)_{1.8}$ -MOF and the number of mesopores of  $Fe_{1.2}(CoNi)_{1.8}S_6$  MES is larger. A large number of mesopores have made a significant contribution to facilitate the electron transport in the OER/ORR progress and to extend catalytic active sites, which results in the enhancement of OER/ORR performance [47].

High-resolution transmission electron microscopy (HRTEM) image further suggests the transformation from amorphous/crystalline structure to highly crystalline nanopaticles (Fig. 1d, e), as verified by the lattice spacing and diffraction patterns (inset of Fig. 1d, e). The as-prepared  $Fe_{1.2}(CoNi)_{1.8}$ -MOF precursor with MOF structure is proved by the selected area electron diffraction (SAED) pattern (inset of Fig. 1d), and the diffraction ring of the (200) and (001) planes are presented. The amorphous phase in HRTEM image proves that the precursor has amorphous structure, which is line in with XRD pattern. In contrast, the corresponding diffraction ring in SAED pattern demonstrates the crystalline nanopaticles of the  $Fe_{1.2}(CoNi)_{1.8}S_6$  MES, which is also consistent with the XRD pattern. HAADF-STEM elemental mapping

images manifest that the Fe, Co, Ni, O and S atoms evenly distribute on the sample, suggesting that  $Fe_{1.2}(CoNi)_{1.8}$ -MOF precursor are sulfured to form  $Fe_{1.2}(CoNi)_{1.8}S_6$  medium-entropy sulfide nanoparticles successfully (Fig. 1f). Similarly, each element is uniformly distributed in the  $Fe_{1.2}(CoNi)_{1.8}$ -MOF precursor, as shown in Fig. S7.

### 3.2. Electrochemical evaluation of OER/ORR performance

The OER performances of  $Fe_x(CoNi)_{3-x}$ -MOFs were measured in  $N_2$ -saturated 1 M KOH electrolyte. The linear sweep voltammetry (LSV) curves were tested at scan rate of  $5\text{ mV s}^{-1}$ , as presented in Fig. 2a. The overpotential of  $Fe_x(CoNi)_{3-x}$ -MOFs electrocatalysts is 282 mV ( $x = 0.6$ ), 280 mV ( $x = 0.8$ ), 269 mV ( $x = 1$ ), 246 mV ( $x = 1.2$ ) and 287 mV ( $x = 1.4$ ) at the current density of  $10\text{ mA cm}^{-2}$ , respectively. Compared with other electrocatalysts, the  $Fe_{1.2}(CoNi)_{1.8}$ -MOF possesses best OER activity accompanied by a low overpotential of 246, 277 and 289 mV at the current densities of 10, 30, and  $50\text{ mA cm}^{-2}$ , respectively (Fig. 2b). The Tafel slope is an important parameter reflecting OER reaction kinetics, which were counted from LSV curve (Fig. 2c). With the value of  $x$  in  $Fe_x(CoNi)_{3-x}$ -MOFs changing from 0.6 to 1.4, the Tafel slope was obtained to be 76, 69, 65, 57 and  $60\text{ mV dec}^{-1}$ , respectively. Moreover, electrochemical impedance spectroscopy (EIS) measurements were manifested in Fig. 2d. The charge transfer resistance ( $R_{ct}$ ) was obtained by fitting the Nyquist diagram with the equivalent circuit model (inset of Fig. 2d).  $R_{ct}$ , CPE, and  $R_1$  stand for charge transfer resistance of the OER process, the electron transport of the catalyst/electrolyte interface, and ohmic resistance (e.g. solution resistance, oxide film resistance, etc.), respectively. It can also be found that  $Fe_{1.2}(CoNi)_{1.8}$ -MOF has smaller charge transfer resistance ( $R_{ct}=63.4\text{ }\Omega$ ) than  $FeCoNi$ -MOF ( $72.0\text{ }\Omega$ ),  $Fe_{0.6}(CoNi)_{2.4}$  ( $145.2\text{ }\Omega$ ),  $Fe_{0.8}(CoNi)_{2.2}$  ( $105.9\text{ }\Omega$ ) and  $Fe_{1.4}(CoNi)_{1.6}$ -MOF ( $141.2\text{ }\Omega$ ), respectively. Smaller charge transfer resistance means higher OER catalytic activity [48]. Fig. 2e shows the double-layer capacitance ( $C_{dl}$ ) of  $Fe_x(CoNi)_{3-x}$ -MOFs, which were used to estimate the electrochemical surface areas (ECSAs).

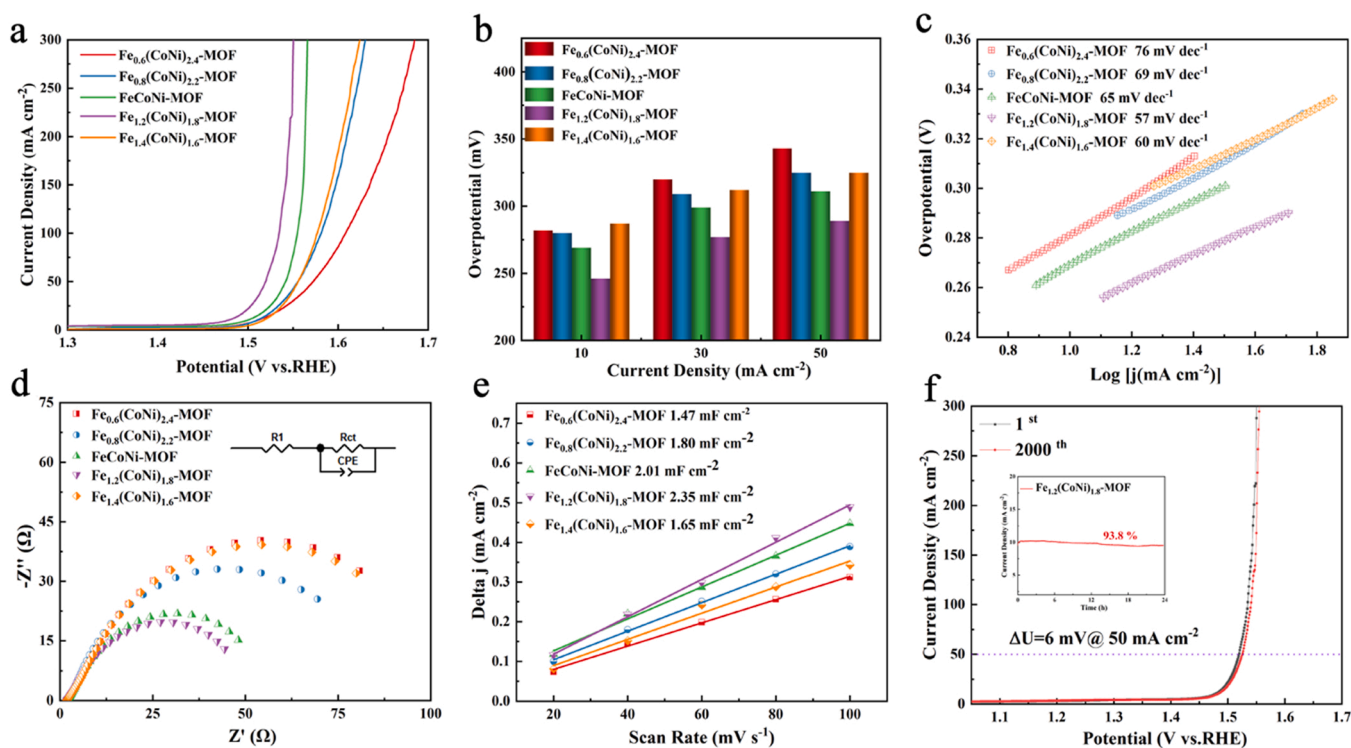


**Fig. 2.** OER performance evaluation of  $Fe_x(CoNi)_{3-x}$ -MOFs in alkaline environment. (a) LSV curves. (b) Comparison of overpotential at the  $10\text{ mA cm}^{-2}$ ,  $30\text{ mA cm}^{-2}$  and  $50\text{ mA cm}^{-2}$ . (c) Tafel plots. (d) EIS Nyquist plots. (e) Double-layer capacitance obtained by the current density at different scan rates. (f) LSV polarization curves of  $Fe_{1.2}(CoNi)_{1.8}$ -MOF before and after 2000 CV cycles for stability test. Inset is 24 h chronoamperometry curves.



The original data were obtained from the cyclic voltammograms (CVs) at different rates within the non-faradic voltage (Fig. S8). The ECSAs can be calculated from the equation  $ECSA = S \times C_{dl}/C_s$  [49], as presented in Fig. S9. The results show that the ECSA of  $Fe_{1.2}(CoNi)_{1.8}$ -MOF is  $58.8 \text{ cm}^2$ , which presents highest value among  $Fe_x(CoNi)_{3-x}$ -MOFs. The above results manifest the disparity in the quantity of active sites among the  $Fe_x(CoNi)_{3-x}$ -MOFs with different ratio of elements.

$Fe_{1.2}(CoNi)_{1.8}$ -MOF can not only possess high OER catalytic activity, but also maintains certain stability. Fig. 2f shows the LSV curve of the  $Fe_{1.2}(CoNi)_{1.8}$ -MOF electrode after 2000 CV cycles at scan rate of  $50 \text{ mV s}^{-1}$  compared with the original LSV curve, which expressed  $\Delta U = 6 \text{ mV}$  at the current density of  $50 \text{ mA cm}^{-2}$ . Moreover, the stability of the  $Fe_{1.2}(CoNi)_{1.8}$ -MOF electrode was tested using a long-term chronoamperometry method. The electric current of  $Fe_{1.2}(CoNi)_{1.8}$ -MOF catalyst remained at 93.8% in 24 h in contrast with the original 10 mA, as presented in the inset of Fig. 2f. To further analyze the stability of  $Fe_{1.2}(CoNi)_{1.8}$ -MOF, the microstructure and elemental distribution of sample were obtained by HAADF-STEM image and corresponding elemental mapping (Fig. S10) after the 24 h chronoamperometry. Compared with the elemental mappings of  $Fe_{1.2}(CoNi)_{1.8}$ -MOF before

24 h stability test, the elemental mappings of  $Fe_{1.2}(CoNi)_{1.8}$ -MOF remain the uniform distributions of all the elements after stability test. From what has been discussed above,  $Fe_{1.2}(CoNi)_{1.8}$ -MOF has high catalytic activity and stability, which would be selected as precursor to be sulfuretted in different degrees.

The OER performance of the optimal  $Fe_{1.2}(CoNi)_{1.8}$ -MOF precursors and  $Fe_{1.2}(CoNi)_{1.8}S_x$  MES nanoparticles was examined in same alkaline environment. The LSV curves of  $Fe_{1.2}(CoNi)_{1.8}$ -MOF precursors and  $Fe_{1.2}(CoNi)_{1.8}S_x$  MES nanoparticles are displayed in Fig. 3a. The results show that  $Fe_{1.2}(CoNi)_{1.8}S_6$  exhibits the highest OER activity accompanied by the lowest overpotential, which was only 276 mV at a current density of  $100 \text{ mA cm}^{-2}$ , compared with  $Fe_{1.2}(CoNi)_{1.8}$ -MOF ( $\eta_{100} = 305 \text{ mV}$ ),  $Fe_{1.2}(CoNi)_{1.8}S_3$  ( $\eta_{100} = 291 \text{ mV}$ ) and  $Fe_{1.2}(CoNi)_{1.8}S_9$  ( $\eta_{100} = 282 \text{ mV}$ ). Compared with other electrocatalysts, the  $Fe_{1.2}(CoNi)_{1.8}S_6$  owns best OER activity with a low overpotential of 260, 276 and 293 mV at the current densities of 50, 100, and  $200 \text{ mA cm}^{-2}$ , respectively (Fig. 3b). In addition, the Tafel slope can be used as an important parameter to measure the reaction kinetic. As presented in Fig. 3c, the Tafel slope of  $Fe_{1.2}(CoNi)_{1.8}S_6$  is  $53 \text{ mV dec}^{-1}$ , which is smaller than  $Fe_{1.2}(CoNi)_{1.8}$ -MOF ( $57 \text{ mV dec}^{-1}$ ),  $Fe_{1.2}(CoNi)_{1.8}S_3$  ( $55 \text{ mV dec}^{-1}$ ) and

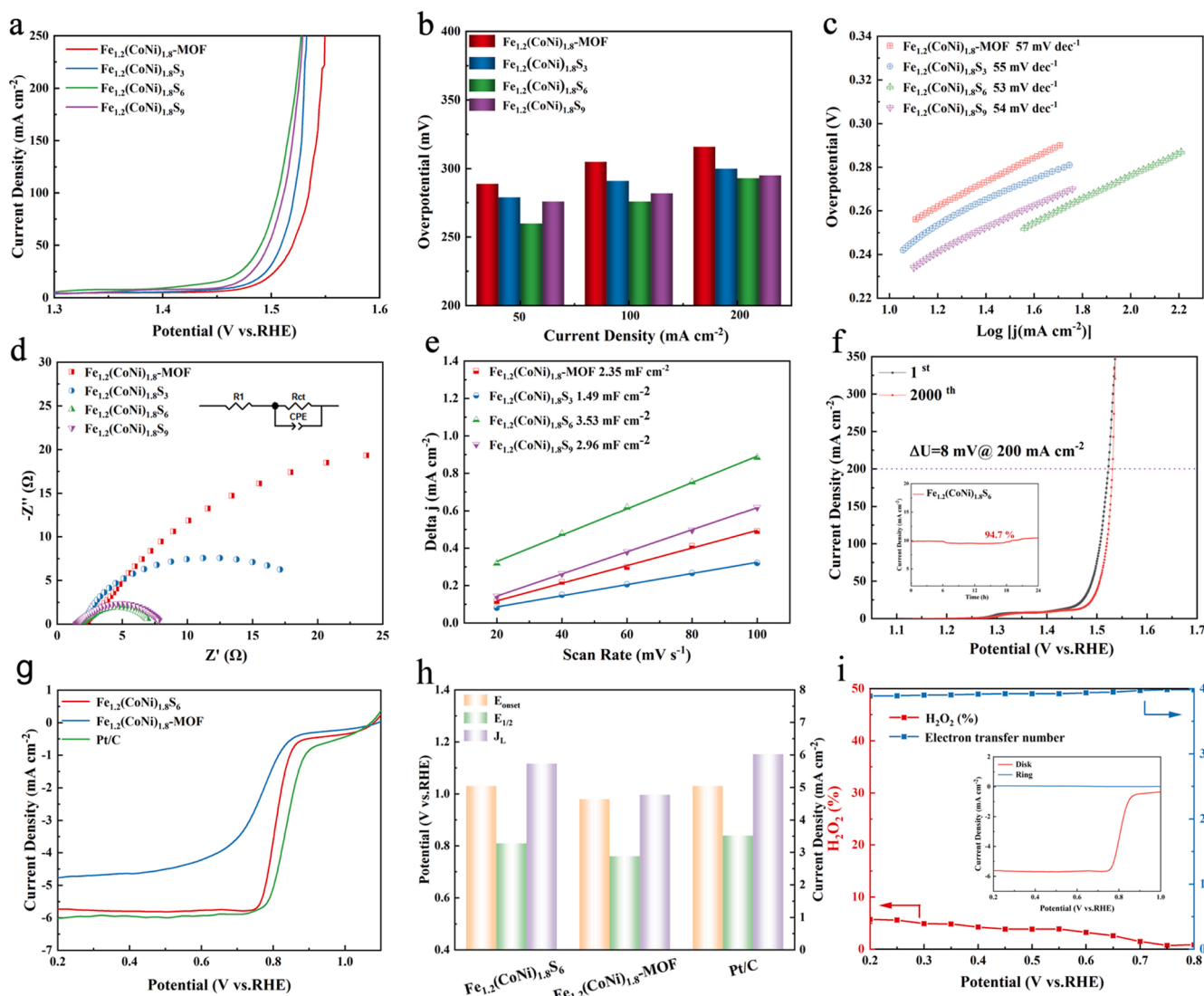


**Fig. 3.** OER/ORR performance evaluation of  $Fe_{1.2}(CoNi)_{1.8}S_x$  MESs in alkaline environment. (a) OER LSV curves. (b) Comparison of overpotential at the  $50 \text{ mA cm}^{-2}$ ,  $100 \text{ mA cm}^{-2}$  and  $200 \text{ mA cm}^{-2}$ . (c) Tafel plots. (d) EIS Nyquist plots. (e) Double-layer capacitance obtained by the current density at different scan rates. (f) LSV polarization curves of  $Fe_{1.2}(CoNi)_{1.8}S_6$  before and after 2000 CV cycles for stability test. Inset is 24 h chronoamperometry curves. (g) ORR LSV curves. (h) Comparison of  $E_{onset}$ ,  $E_{1/2}$  and  $J_L$ . (i) RRDE lines of  $H_2O_2$  yield (%) and electron transfer number ( $n$ ) of  $Fe_{1.2}(CoNi)_{1.8}S_6$ .

$\text{Fe}_{1.2}(\text{CoNi})_{1.8}\text{S}_9$  ( $54 \text{ mV dec}^{-1}$ ). Sulfur-doping can adjust the electronic structure of metallic elements, which accelerates the synergistic effect between multiple elements [50]. To verify the effect of the carrier, the LSV curves of  $\text{Fe}_{1.2}(\text{CoNi})_{1.8}\text{S}_6$  loaded nickel foam and the bare NF are exhibited in Fig. S11, showing that bare NF manifested negligible OER activity, and the OER performance of  $\text{Fe}_{1.2}(\text{CoNi})_{1.8}\text{S}_6$  is clearly better than that of commercial  $\text{RuO}_2$  noble-metal oxide. Compared with the OER performance of the reported medium/high entropy materials,  $\text{Fe}_{1.2}(\text{CoNi})_{1.8}\text{S}_6$  MESs nanoparticles have better performance, which can be seen in Table S2. For comparison, the LSV curves of  $\text{Fe}_{1.2}(\text{Cr-CoNiCu})_{1.8}\text{S}_6$ ,  $\text{Fe}_{1.2}(\text{CoNiCu})_{1.8}\text{S}_6$ ,  $\text{Fe}_{1.2}(\text{CoNi})_{1.8}\text{S}_6$  and  $\text{Fe}_{1.2}\text{Ni}_{1.8}\text{S}_6$  are shown in Fig. S12. The catalytic activity first increased and then decreased with the increase of the number of principal elements. It is obvious that the activity of the ternary medium-entropy sulfide is higher than that of the quinary high-entropy sulfide.

Besides, electrical conductivity has a great influence on catalytic activity and the impedance of  $\text{Fe}_{1.2}(\text{CoNi})_{1.8}\text{S}_x$  MESs nanoparticles is investigated with EIS experiments, as presented in Fig. 3d. For these as-prepared catalysts,  $\text{Fe}_{1.2}(\text{CoNi})_{1.8}\text{S}_6$  MES shows the lowest  $R_{\text{ct}}$  of  $5.9 \Omega$

compared to  $\text{Fe}_{1.2}(\text{CoNi})_{1.8}\text{-MOF}$  ( $R_{\text{ct}}=63.4 \Omega$ ),  $\text{Fe}_{1.2}(\text{CoNi})_{1.8}\text{S}_3$  ( $R_{\text{ct}}=27.8 \Omega$ ) and  $\text{Fe}_{1.2}(\text{CoNi})_{1.8}\text{S}_9$  ( $R_{\text{ct}}=6.6 \Omega$ ), which further illustrate the excellent charge transfer capability. Additionally, the ECSA was used to evaluate the intrinsic activity of  $\text{Fe}_{1.2}(\text{CoNi})_{1.8}\text{S}_x$  MESs nanoparticles electrocatalysts. As we know from the above, ECSA can be obtained from the  $C_{\text{dl}}$  according to the related formula. The difference in current density was plotted in different scan rate (Fig. S13), and the value of  $C_{\text{dl}}$  are counted by the related slope (Fig. 3e). As a result, the ECSA obtained are 58.8, 37.3, 88.3 and  $74.0 \text{ cm}^2$  for  $\text{Fe}_{1.2}(\text{CoNi})_{1.8}\text{-MOF}$  precursor,  $\text{Fe}_{1.2}(\text{CoNi})_{1.8}\text{S}_3$ ,  $\text{Fe}_{1.2}(\text{CoNi})_{1.8}\text{S}_6$  and  $\text{Fe}_{1.2}(\text{CoNi})_{1.8}\text{S}_9$ , respectively (Fig. S14). It is obvious that  $\text{Fe}_{1.2}(\text{CoNi})_{1.8}\text{S}_6$  has the largest value of  $C_{\text{dl}}$ , suggesting that it provides more active sites to enhance OER performance.

The long-term OER stability of optimum  $\text{Fe}_{1.2}(\text{CoNi})_{1.8}\text{S}_6$  MES electrode was assessed by means of continuous CV cycling at the scan rate of  $50 \text{ mV s}^{-1}$  for 2000 cycles. The LSV curves after 2000 cycles are presented in Fig. 4f. After 2000 cycles, the voltage difference between the 2000 CV cycles and original curve is only 8 mV at the current density of  $200 \text{ mA cm}^{-2}$ . This indicates the excellent OER stability of the

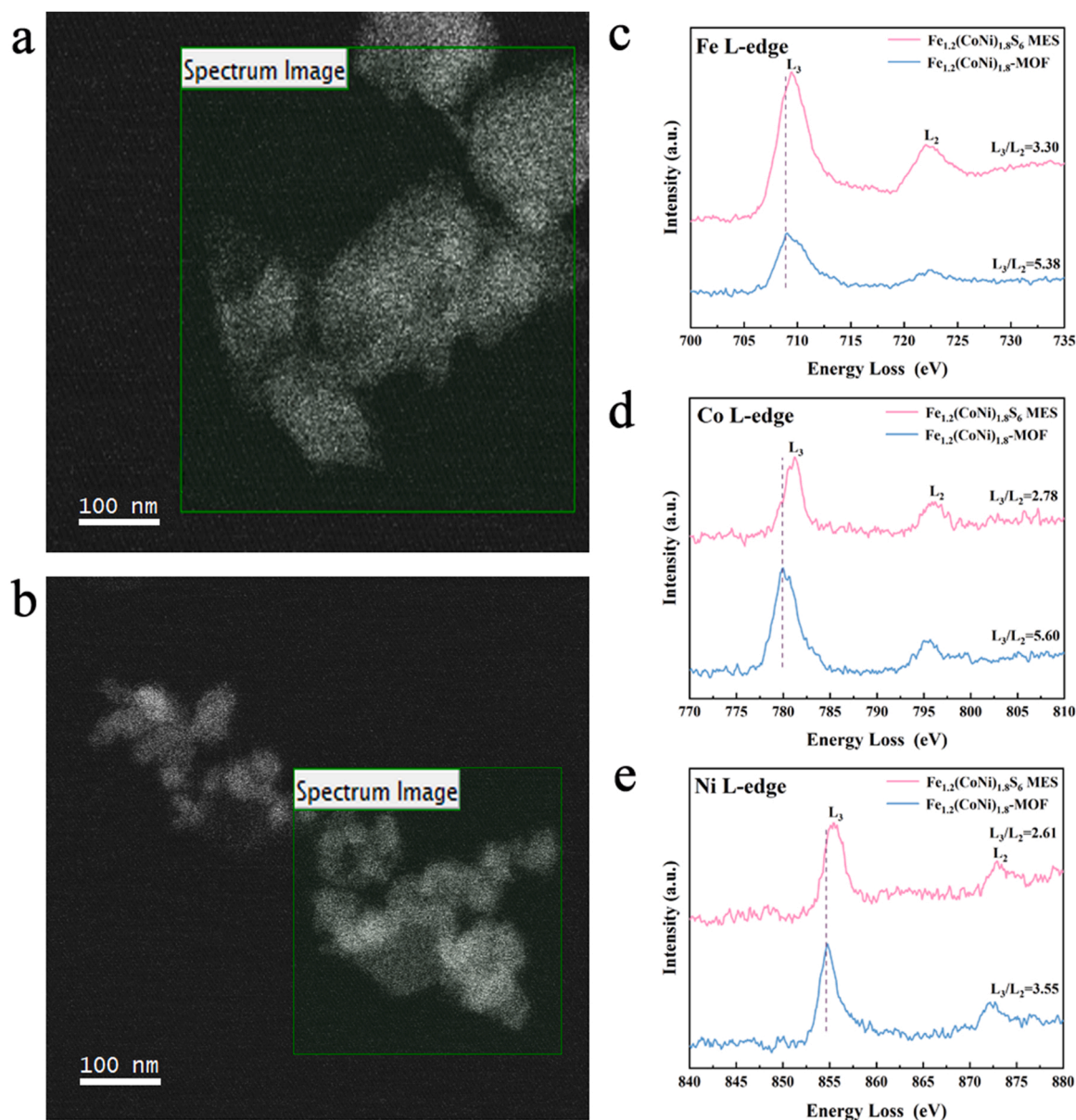


Fig. 4. STEM images of (a)  $\text{Fe}_{1.2}(\text{CoNi})_{1.8}\text{-MOF}$  and (b)  $\text{Fe}_{1.2}(\text{CoNi})_{1.8}\text{S}_6$  MES, and corresponding EELS spectrum of (c) Fe L-edge; (d) Co L-edge and (e) Ni L-edges.

$\text{Fe}_{1.2}(\text{CoNi})_{1.8}\text{S}_6$  MES electrode. The OER stability of the  $\text{Fe}_{1.2}(\text{CoNi})_{1.8}\text{S}_6$  MES is ascribed to the synergistic effect of medium entropy configuration [27]. The MES electrocatalyst was further assessed for the durability. The 24 h durability test consequence obtained at the  $10 \text{ mA cm}^{-2}$  is displayed in the inset of Fig. 3 f. Compared to  $\text{Fe}_{1.2}(\text{CoNi})_{1.8}\text{-MOF}$  ( $\sim 93.8\%$ ), the  $\text{Fe}_{1.2}(\text{CoNi})_{1.8}\text{S}_6$  MES remained 94.7% after 24 h durability test, suggesting better durability. Such outstanding stability implies that the MES electrocatalyst is relatively steady during the OER in 1 M KOH electrolyte. The XRD pattern of  $\text{Fe}_{1.2}(\text{CoNi})_{1.8}\text{S}_6$  MES after 2000 CV cycles and after 24 h durability test displays the similar diffraction peaks with original  $\text{Fe}_{1.2}(\text{CoNi})_{1.8}\text{S}_6$  (Fig. S15). Except for the peaks of nickel foam ( $44.3^\circ$ ,  $51.8^\circ$  and  $76.4^\circ$ ), the peaks at  $30.9^\circ$ ,  $50.1^\circ$  and  $55.3^\circ$  are assigned to medium-entropy metal sulfides. After 2000 CV cycles or 24 h durability test, the new peaks appeared ( $37.7^\circ$  and  $49.6^\circ$ ), which may be the formation of metal oxyhydroxides during OER [27]. After 2000 CV cycles and after 24 h durability test, the microstructure and elemental distribution of  $\text{Fe}_{1.2}(\text{CoNi})_{1.8}\text{S}_6$  MES were obtained by HAADF-STEM image and corresponding elemental mapping, as observed in Fig. S16, S17. It can be seen that there is no significant change of structure and all the elemental mappings of  $\text{Fe}_{1.2}(\text{CoNi})_{1.8}\text{S}_6$  MES remain the uniform distribution. On the one hand, the oxidation resistance of Ni contributes to the excellent oxidation resistance of  $\text{Fe}_{1.2}(\text{CoNi})_{1.8}\text{S}_6$  medium-entropy system. On the other hand, the multi-principal elements (Fe/Co/Ni) can generate compact passivation layer to stop further oxidation. To sum up, the cocktail effect of the medium-entropy system was beneficial to the dense passivation layer, thus preventing the further oxidation of the metal components. Additionally, the unique medium-entropy structure of  $\text{Fe}_{1.2}(\text{CoNi})_{1.8}\text{S}_6$  MES lowers the Gibbs free energy of the system to improve the stability of the system.

In addition to the OER catalytic performance, the oxygen reduction reaction (ORR) catalytic performance of the electrocatalyst is also an important index cathode catalyst for rechargeable zinc-air batteries. The ORR performances of  $\text{Fe}_{1.2}(\text{CoNi})_{1.8}\text{-MOF}$ ,  $\text{Fe}_{1.2}(\text{CoNi})_{1.8}\text{S}_6$  MES and commercial catalysts 20 wt% Pt/C were measured in  $\text{O}_2$ -saturated 0.1 M KOH electrolyte. Fig. 3 g shows the ORR LSV curves of the samples at 1600 rpm. As presented in Fig. 3 h, the diffusion-limited current density ( $J_L$ ) of the  $\text{Fe}_{1.2}(\text{CoNi})_{1.8}\text{-MOF}$  precursor was  $4.77 \text{ mA cm}^{-2}$  (0.2 V), and the onset potential ( $E_{\text{onset}}$ ) and half-wave potential ( $E_{1/2}$ ) were 0.98 V and 0.76 V, respectively. The  $J_L$ ,  $E_{\text{onset}}$  and  $E_{1/2}$  of  $\text{Fe}_{1.2}(\text{CoNi})_{1.8}\text{S}_6$  MES were  $5.73 \text{ mA cm}^{-2}$ , 1.03 V and 0.81 V, respectively. Compared with the precursor, the  $J_L$ ,  $E_{\text{onset}}$  and  $E_{1/2}$  were increased, even close to Pt/C (the  $J_L$ ,  $E_{\text{onset}}$  and  $E_{1/2}$  were  $6.02 \text{ mA cm}^{-2}$ , 1.03 V and 0.84 V, respectively), indicating that the formation of medium-entropy sulfide nanoparticles can improve the ORR catalytic activity. Among  $\text{Fe}_{1.2}(\text{CoNi})_{1.8}\text{S}_x$  MESs electrocatalysts,  $\text{Fe}_{1.2}(\text{CoNi})_{1.8}\text{S}_6$  MES presented the best ORR activity, as displayed in Fig. S18. The Tafel plots of catalysts endorse enhanced ORR catalytic kinetics of  $\text{Fe}_{1.2}(\text{CoNi})_{1.8}\text{S}_6$  MES, owing to the synergetic coupling of medium-entropy sulfide, where the value Tafel slope of  $\text{Fe}_{1.2}(\text{CoNi})_{1.8}\text{S}_6$  MES is  $78 \text{ mV dec}^{-1}$ , which is lower than MOF precursor ( $146 \text{ mV dec}^{-1}$ ) and Pt/C ( $99 \text{ mV dec}^{-1}$ ), as shown in Fig. S19. Compared with the ORR performance of the reported catalysts,  $\text{Fe}_{1.2}(\text{CoNi})_{1.8}\text{S}_6$  MESs nanoparticles have better performance, which can be seen in Table S3. In order to study the kinetic process of ORR, the LSV curve of  $\text{Fe}_{1.2}(\text{CoNi})_{1.8}\text{S}_6$  MES at 400–2050 rpm was tested by RDE (Fig. S20). As displayed in inset of Fig. S17, the corresponding K-L curves can be obtained by fitting LSV curves at 0.2, 0.25, 0.3, 0.35 and 0.4 V with different rotational speeds. According to the slope of the curve, the electron transfer number calculated by the K-L equation are between 3.84 and 3.98. RRDE was further used to perform LSV curves of  $\text{Fe}_{1.2}(\text{CoNi})_{1.8}\text{S}_6$  MES, as shown in Fig. 3i. Based on the disk current and ring current, the yield of the secondary reaction intermediate  $\text{H}_2\text{O}_2$  and transfer electron number (3.89–3.98) were calculated. The above results are consistent with those calculated by K-L equation, which indicate that the ORR process of  $\text{Fe}_{1.2}(\text{CoNi})_{1.8}\text{S}_6$  MES is an ideal four-electron process. The ORR stability of  $\text{Fe}_{1.2}(\text{CoNi})_{1.8}\text{S}_6$  MES was further tested, as

presented in Fig. S21. The current density of  $\text{Fe}_{1.2}(\text{CoNi})_{1.8}\text{S}_6$  MES at 0.75 V potential remained 88.2% at 1600 rpm during 12 h, which demonstrated the high stability of MES during ORR process. Similarly, there are no obvious changes for the HAADF-STEM image and corresponding elemental mapping of  $\text{Fe}_{1.2}(\text{CoNi})_{1.8}\text{S}_6$  MES in Fig. S22, suggesting the splendid structural stability.

To compare the structural characteristics and electrochemical performance with that of pure  $\text{Fe}_{1.2}(\text{CoNi})_{1.8}\text{S}_6$  and  $\text{Fe}_{1.2}(\text{CoNi})_{1.8}\text{S}_6$  MES catalysts, the specific preparation method is as follows. Fe-MOF, Co-MOF and Ni-MOF were prepared via the same ultrasonic method. Fe-MOF, Co-MOF and Ni-MOF were sulfured into metal sulfides (metal = Fe/Co/Ni) by hydrothermal method under the same proportion as  $\text{Fe}_{1.2}(\text{CoNi})_{1.8}\text{S}_6$  MES. Finally, pure  $\text{Fe}_{1.2}(\text{CoNi})_{1.8}\text{S}_6$  was obtained by mixing the above metal sulfides. Fig. S23 shows the XRD patterns of pure  $\text{Fe}_{1.2}(\text{CoNi})_{1.8}\text{S}_6$ . It can be seen that there are obvious peaks of different metal sulfides. Additionally, it can be found that the distribution of the three metal elements is not uniform through the HAADF-STEM image and corresponding elemental mapping (Fig. S24), which demonstrates the generation of pure  $\text{Fe}_{1.2}(\text{CoNi})_{1.8}\text{S}_6$ . The OER LSV curves of pure  $\text{Fe}_{1.2}(\text{CoNi})_{1.8}\text{S}_6$  and  $\text{Fe}_{1.2}(\text{CoNi})_{1.8}\text{S}_6$  MES are displayed in Fig. S25a. Obviously, the OER activity of  $\text{Fe}_{1.2}(\text{CoNi})_{1.8}\text{S}_6$  MES is better than that of pure  $\text{Fe}_{1.2}(\text{CoNi})_{1.8}\text{S}_6$ . Fig. S25b shows the ORR LSV curve of pure  $\text{Fe}_{1.2}(\text{CoNi})_{1.8}\text{S}_6$ . Compared with  $\text{Fe}_{1.2}(\text{CoNi})_{1.8}\text{S}_6$  MES, the pure  $\text{Fe}_{1.2}(\text{CoNi})_{1.8}\text{S}_6$  exhibits lower ORR activity along with a  $J_L$  of  $5.18 \text{ mA cm}^{-2}$  and  $E_{1/2}$  of 0.77 V. The superb catalytic activity and durability of the as-prepared MES root in the nature of the medium-entropy configuration. As the variety of alloying elements increases, the possibility of forming complex compounds also increases, which signifies that higher driving forces are demanded to overcome the oxygen evolution reaction energy barriers [51,52]. However, the medium/high-entropy configuration tends to form a simple solid solution, which can take the structural advantages to enhance catalytic properties. The three alloying elements (Fe/Co/Ni) in this work not only have good catalytic performance, but also have the small difference in electronegativity, the similar valence states and the small difference in atomic size, which is beneficial to form a simple solid solution to further improve catalytic performance. Specifically, the improvement of OER performance is mainly attributed to two aspects, namely, the formation of nanoparticles in morphology and the regulation of electronic structure. The morphology of nanoparticles with large surface area can improve the OER performance. Regulation of electronic structure are discussed in the following sections through electron energy loss spectroscopy (EELS), X-ray photoelectron spectroscopy (XPS) and density functional theory (DFT) in detail.

### 3.3. Electron valence analysis

The chemical state of catalysts were analyzed by EELS spectrum. EELS spectrum of  $\text{Fe}_{1.2}(\text{CoNi})_{1.8}\text{-MOF}$  and  $\text{Fe}_{1.2}(\text{CoNi})_{1.8}\text{S}_6$  MES are shown in Fig. 4. Fig. 4a,b display the selected images (obtained from spherical aberration-corrected STEM images) of  $\text{Fe}_{1.2}(\text{CoNi})_{1.8}\text{-MOF}$  and  $\text{Fe}_{1.2}(\text{CoNi})_{1.8}\text{S}_6$  MES, respectively. And the L-edge spectra of the three metallic elements before and after sulfuration are presented in Fig. 4c-e. It can be observed that the  $L_3$  edge of Fe, Co and Ni elements in  $\text{Fe}_{1.2}(\text{CoNi})_{1.8}\text{S}_6$  MES shift significantly to the right compared with  $\text{Fe}_{1.2}(\text{CoNi})_{1.8}\text{-MOF}$  precursor. This indicates that the valence state increases when the metallic element in precursor is oxidized. Furthermore, the  $L_3/L_2$  ratio of the Fe, Co and Ni elements are 5.38, 5.60 and 3.55 in the precursor, respectively. After the formation of MES by sulfuration, the above data are reduced to 3.30, 2.78 and 2.61, indicating the transformation from  $\text{Fe}^{2+}$  to  $\text{Fe}^{3+}$ ,  $\text{Co}^{2+}$  to  $\text{Co}^{3+}$  and  $\text{Ni}^{2+}$  to  $\text{Ni}^{3+}$  possibly [53,54]. The transition metallic elements with high valence states exhibit superior catalytic activities [55,56]. The increased holes in d-band of oxidized metal species with high valence can enhance the covalency of metal-oxygen (M-O) bonds to promote the charge transfer. In addition, high valence states typically induce the downshift of metal



d-band to overlap p-band of oxygen ligands, which can lower the limiting energy barrier to accelerate oxygen evolution reaction kinetics [56].

It is indispensable to observe the surface electrochemical states of  $\text{Fe}_{1.2}(\text{CoNi})_{1.8}\text{-MOF}$  and  $\text{Fe}_{1.2}(\text{CoNi})_{1.8}\text{S}_6$  MES because the electrochemical activity of catalysts is dominated by electrochemical states. The XPS survey spectrum of  $\text{Fe}_{1.2}(\text{CoNi})_{1.8}\text{S}_6$  MES clearly displays the presence of Fe, Co, Ni, C, O and S, as obtained from Fig. 5. In addition, it can be further demonstrated that the  $\text{Fe}_{1.2}(\text{CoNi})_{1.8}\text{-MOF}$  precursor is sulfurized into  $\text{Fe}_{1.2}(\text{CoNi})_{1.8}\text{S}_6$  medium-entropy sulfide successfully. The Fe 2p spectrum of  $\text{Fe}_{1.2}(\text{CoNi})_{1.8}\text{-MOF}$  and  $\text{Fe}_{1.2}(\text{CoNi})_{1.8}\text{S}_6$  MES are manifested in Fig. 5b. For the  $\text{Fe}_{1.2}(\text{CoNi})_{1.8}\text{-MOF}$  precursor, Fe  $2p_{3/2}$  and Fe  $2p_{1/2}$  peaks located at 712.3 and 724.0 eV, corresponding to  $\text{Fe}^{2+}$  [57]. Compared to the precursor,  $\text{Fe}_{1.2}(\text{CoNi})_{1.8}\text{S}_6$  MES reveals the new peaks, namely Fe-S at 707.3 eV and  $\text{Fe}^{3+}$  at 712.8 eV [58,59]. Moreover, the peaks centering at 710.9 and 715.1 eV are belong to  $\text{Fe}^{2+}$  and satellite peaks [60]. As shown by the high-resolution Co 2p spectra in Fig. 5c, the Co  $2p_{3/2}$  peak can be deconvoluted into two peaks at 782.0 and 778.4 eV, which allotted to  $\text{Co}^{2+}$  and  $\text{Co}^{3+}$  in the  $\text{Fe}_{1.2}(\text{CoNi})_{1.8}\text{S}_6$  MES [61]. Similarly, the Co  $2p_{1/2}$  peak can be deconvoluted into two peaks at 797.3 and 793.5 eV, which allotted to  $\text{Co}^{2+}$  and  $\text{Co}^{3+}$ . In addition, the peaks at 786.1 eV and 803.8 eV are determined to the satellite peaks [62]. It's worth noting that the high valence  $\text{Co}^{3+}$  species can modulate the electron density and promote the OER activity [46, 63]. In the Ni 2p XPS spectra of the  $\text{Fe}_{1.2}(\text{CoNi})_{1.8}\text{S}_6$  MES (Fig. 5d), the binding energies at 853.2, 856.1, 857.0 and 861.1 eV can be assigned to Ni-S,  $\text{Ni}^{2+}$ ,  $\text{Ni}^{3+}$  and satellite peak, respectively [58,64]. For comparison, main characteristic peaks at 856.3 eV and satellite at 861.6 eV manifest the existence of only  $\text{Ni}^{2+}$  species in the  $\text{Fe}_{1.2}(\text{CoNi})_{1.8}\text{-MOF}$  precursor. In general, according to the XPS results,  $\text{M}^{2+}$  ( $\text{M} = \text{Fe/Co/Ni}$ ) transition to higher valence states after the formation of MES, which contributes to the improvement of electro-catalytic performance [55,56, 65]. In addition, compared with  $\text{Fe}_{1.2}(\text{CoNi})_{1.8}\text{-MOF}$  precursor, the peaks of  $\text{Fe}^{2+}$  and  $\text{Ni}^{2+}$  in  $\text{Fe}_{1.2}(\text{CoNi})_{1.8}\text{S}_6$  MES shift to lower binding

energy, implying that Fe and Ni elements play the role as electron-rich states in the medium-entropy system. On the contrary, Co element assumes the role of electron-deficient states. Therefore, it can infer that the electron deficient Co acts as electron donors for the electron rich Fe and Ni, motivating strong-electronic synergistic effect to enhance OER performance [26]. As for O 1s XPS spectrum of  $\text{Fe}_{1.2}(\text{CoNi})_{1.8}\text{-MOF}$  precursor in Fig. 5e, two characteristic peaks located at 531.5 and 532.3 eV are assigned to M-O and surface adsorbed water ( $\text{H}_2\text{O}_{\text{ads}}$ ) [66]. Compared to the precursor,  $\text{Fe}_{1.2}(\text{CoNi})_{1.8}\text{S}_6$  MES manifests the new peaks, that is,  $\text{SO}_4^{2-}$  at 532.2 eV. The high resolution S 2p spectrum (Fig. 5f) is deconvoluted into three components centered at 161.6, 162.8 and 168.8 eV, corresponding to assigned to  $2p_{3/2}$  (M-S),  $2p_{1/2}$  (M-S) and  $\text{SO}_4^{2-}$ , respectively [67,68]. It is worth noting that  $\text{SO}_4^{2-}$  at 168.8 eV corresponds to the O 1s spectrum in Fig. 5f, which coexists with metal species to conduce to the improvement of OER performance [68].

Furthermore, in order to analyze the chemical behavior of Fe, Co and Ni atoms, the XPS analysis was offered to explain the chemical state evolution of  $\text{Fe}_{1.2}(\text{CoNi})_{1.8}\text{S}_6$  MES (Fig. S26). After the 24 h OER test, the Fe, Co, Ni, and O spectra were different from those of the initial specimen (Fig. 5b-e). As for the Fe 2p spectrum, part of  $\text{Fe}^{2+}$  was oxidized to  $\text{Fe}^{3+}$  after the 24 h OER test, suggesting that the initial metallic centers might oxidize to the higher valence state during OER. In regard to the Co 2p and Ni 2p XPS spectrum, the similar phenomenon was also observed. The reason for this phenomenon is that the Fe/Co/Ni sites readily accept the hydroxyl under alkaline condition and form metal (oxygen) hydroxides on the surface, which was consistent with the previous XRD tests (Fig. S15). The newly formed metal (oxygen) hydroxides were deemed to enhance the OER activity [37]. In the O 1s spectrum, it was obtained that the newly peak (M-OH) appeared in the spectrum, which was attributed to OH of the hydroxide or (oxygen) hydroxide [68]. Compared to initial sample, the peak of M-O also has a negative shift in the O 1s spectrum, which may be put down to the formation of the M-OOH bond [37]. The significant change of O 1s spectrum demonstrated the oxidation reaction on the surface during OER test.

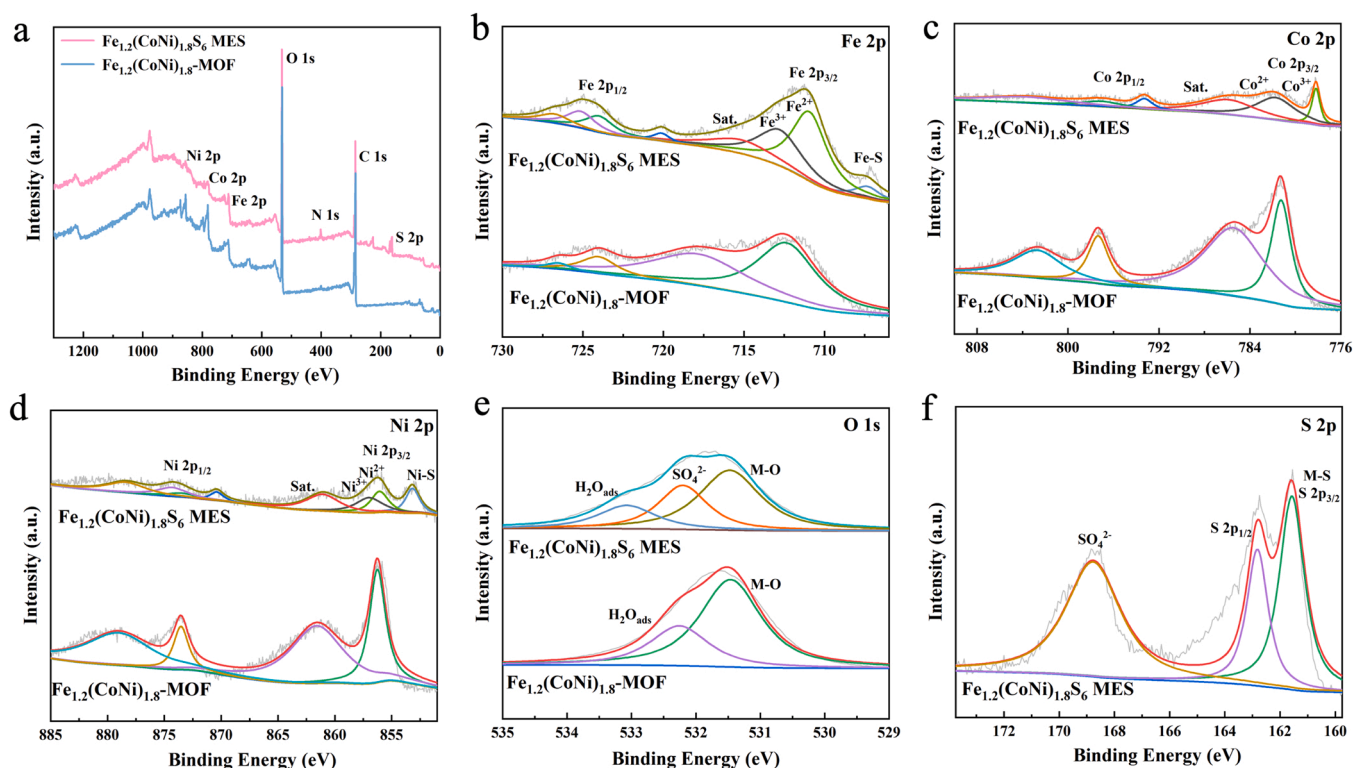
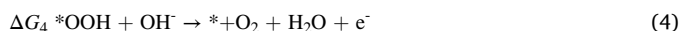
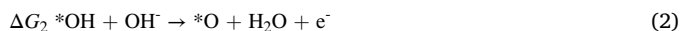


Fig. 5. (a) XPS survey spectra of  $\text{Fe}_{1.2}(\text{CoNi})_{1.8}\text{-MOF}$  and  $\text{Fe}_{1.2}(\text{CoNi})_{1.8}\text{S}_6$  MES, and high-resolution XPS spectra of (b) Fe 2p, (c) Co 2p, (d) Ni 2p, (e) O 1s and (f) S 2p.

### 3.4. Theoretical calculation based on DFT

DFT calculations were implemented to further clarify the catalytic mechanism of  $\text{Fe}_{1.2}(\text{CoNi})_{1.8}\text{S}_6$  medium-entropy sulfide in detail. The optimized configurations of  $\text{Fe}_{1.2}(\text{CoNi})_{1.8}\text{-MOF}$  (200) surfaces and  $\text{Fe}_{1.2}(\text{CoNi})_{1.8}\text{S}_6$  MES (−212) surfaces were displayed in Fig. S27, S28. The Gibbs free energies were computed on account of 4e-transfer mechanism via the DFT calculations [39].



where \* represent active sites in the crystal plane of electrocatalysts, and  $\Delta G_1$ ,  $\Delta G_2$ ,  $\Delta G_3$ , and  $\Delta G_4$  donate the Gibbs free energies of the above reactions, as manifested in Fig. 6a. The Gibbs free energies for the OER process at potential of zero are calculated in Fig. 6b. The highest Gibbs free energy difference of reaction process is known as the rate-determining step (RDS) [37]. It can be clearly obtained that the RDS for  $\text{Fe}_{1.2}(\text{CoNi})_{1.8}\text{-MOF}$  precursor is the formation of  $*\text{OH}$  due to the highest free energy change of 2.63 eV from the results of calculation. Subsequently, after optimal sulfuration, the new RDS of  $\text{Fe}_{1.2}(\text{CoNi})_{1.8}\text{S}_6$  MES becomes the formation of  $*\text{O}$  from  $*\text{OH}$  with a lowered energy change of 1.82 eV. Obviously, the RDS for  $\Delta G$  of  $\text{Fe}_{1.2}(\text{CoNi})_{1.8}\text{S}_6$  MES is lower than that of  $\text{Fe}_{1.2}(\text{CoNi})_{1.8}\text{-MOF}$  precursor, which implies that the OER activity of  $\text{Fe}_{1.2}(\text{CoNi})_{1.8}\text{S}_6$  MES is better than precursor. This conclusion is consistent with the above experimental results. The low  $\Delta G$  manifests that the reaction dynamics are ameliorated on the surface of  $\text{Fe}_{1.2}(\text{CoNi})_{1.8}\text{S}_6$  MES because of the reduced energy barrier, which contributes to enhance OER catalytic performance [69].

Besides, the electronic structure of the electrocatalysts will be regulated to enhance OER catalytic performance after sulfuration [68]. The charge density difference diagram displays the charge redistribution of adsorbed intermediate on interface, indicating the change in charge transfer procedure before and after sulfuration (Fig. S29, S30). It is obvious that the electron distribution on the reconstructed surface of MES is denser than that of the precursor, which manifests that the fast electron transfer can promote the bonding of the O-OH bond efficiently [37,70]. In order to further analyze the charge transfer intuitively, the 2D-plane charge density difference  $\Delta\rho$  was obtained along the z direction in Fig. 6c. Compared with the  $\text{Fe}_{1.2}(\text{CoNi})_{1.8}\text{-MOF}$  precursor, the charge density of  $\text{Fe}_{1.2}(\text{CoNi})_{1.8}\text{S}_6$  MES has a larger positive and negative difference, indicating that more electrons accumulate around the adsorbed intermediate to promote catalytic activity.

The density of states (DOS) as an important parameter affects the catalytic performance in the electronic structure, which can be divided into total density of states (TDOS) and partial density of states (PDOS) [37,68,69]. The TDOS in Fig. 6d suggests that  $\text{Fe}_{1.2}(\text{CoNi})_{1.8}\text{S}_6$  MES has a significant increased TDOS approaching the Fermi level than that of  $\text{Fe}_{1.2}(\text{CoNi})_{1.8}\text{-MOF}$  precursor, manifesting the higher electrical conductivity of  $\text{Fe}_{1.2}(\text{CoNi})_{1.8}\text{S}_6$  MES. The above result is also consistent with the EIS measurement, as mentioned in Fig. 3d. Furthermore, the TDOS of  $\text{Fe}_{1.2}(\text{CoNi})_{1.8}\text{S}_6$  MES was larger than that of  $\text{Fe}_{1.2}(\text{CoNi})_{1.8}\text{-MOF}$  precursor at the Fermi level, indicating the enhanced electron transport rate during the OER process [71]. The increase of electron transport rate contributes to the enhancement of catalytic performance.

The electronic structures of  $\text{Fe}_{1.2}(\text{CoNi})_{1.8}\text{-MOF}$  precursor and  $\text{Fe}_{1.2}(\text{CoNi})_{1.8}\text{S}_6$  MES can be further investigated via PDOS. Because metal atoms are considered as active sites, the d-band center of metal atoms has an important influence on catalytic activity. The formula of d-band center is as follows [68].

$$\varepsilon_d = \frac{\int_{-\infty}^{\infty} \rho(\varepsilon)\varepsilon d\varepsilon}{\int_{-\infty}^{\infty} \rho(\varepsilon) d\varepsilon} \quad (5)$$

where  $\rho$  is the density of states and  $\varepsilon$  is the energy. The integration process is shown in Fig. S31–33. Based on the above calculation, the d-band center of M atoms (M=Fe/Co/Ni) before and after sulfuration are displayed in Fig. 6e–g. The d-band center of the Fe, Co and Ni elements are −0.44, −0.91 and −1.50 eV in the precursor, respectively. While the formation of MES by sulfuration, the above data are changed to −0.38, −0.71 and −1.32 eV, respectively. The upshifting of d-band center to the Fermi level for  $\text{Fe}_{1.2}(\text{CoNi})_{1.8}\text{S}_6$  MES can regulate the electronic structure of metal sites containing more anti-bonding states as well as higher valence states effectively. The regulation of d-band center strengthens the binding ability of the metal site with active intermediates toward efficient oxygen electrocatalysis. Therefore, the d-band center nearing the Fermi level is expected to enhance OER activity.

The crystal orbital Hamilton populations (COHP) of  $*\text{OH}$  absorbing on  $\text{Fe}_{1.2}(\text{CoNi})_{1.8}\text{-MOF}$  precursor and  $\text{Fe}_{1.2}(\text{CoNi})_{1.8}\text{S}_6$  MES are calculated, as shown in Fig. 6 h,i. The integration of -COHP (-ICOHP) results manifested that the intensity of  $*\text{OH}$  on the Fe site for  $\text{Fe}_{1.2}(\text{CoNi})_{1.8}\text{S}_6$  MES (-ICOHP=2.13) is stronger than that for  $\text{Fe}_{1.2}(\text{CoNi})_{1.8}\text{-MOF}$  (-ICOHP=1.55), suggesting that the easier absorption of  $*\text{OH}$  in the OER process on  $\text{Fe}_{1.2}(\text{CoNi})_{1.8}\text{S}_6$  MES [72]. Furthermore, the electron localized function (ELF) presented the electron in  $*\text{OH}$  of  $\text{Fe}_{1.2}(\text{CoNi})_{1.8}\text{S}_6$  MES are more highly localized (Fig. 6j), which result in the stronger binding energy of  $*\text{OH}$  intermediates with Fe atoms [73].

### 3.5. Electrochemical performance of Zn-air batteries

In order to explore the applications of  $\text{Fe}_{1.2}(\text{CoNi})_{1.8}\text{S}_6$  MES catalyst in rechargeable Zn-air battery, the liquid Zn-air battery was assembled with hydrophobic carbon-cloth loaded with catalyst fines at 1.0  $\text{cm}^2$  as the cathode of the battery, Zn sheet as the anode, and mixed aqueous solution (6 M KOH+0.2 M  $\text{ZnCl}_2$ ) as the electrolyte, as shown in Fig. 7a. In addition, for comparison, the catalyst fines was changed to  $\text{Fe}_{1.2}(\text{CoNi})_{1.8}\text{-MOF}$  precursor and commercial mixture of 20 wt%Pt/C and  $\text{RuO}_2$  (denoted as Pt/C+ $\text{RuO}_2$ ), respectively. It is found that the prepared  $\text{Fe}_{1.2}(\text{CoNi})_{1.8}\text{S}_6$  MES presents a high open-circuit voltage of 1.45 V (Fig. 7b), which is higher than that of the  $\text{Fe}_{1.2}(\text{CoNi})_{1.8}\text{-MOF}$  precursor (1.37 V) and Pt/C+ $\text{RuO}_2$  (1.42 V). Fig. 7c shows the discharge curve and power density curve of the samples. It can be found that the highest power density of  $\text{Fe}_{1.2}(\text{CoNi})_{1.8}\text{S}_6$  is 124  $\text{mW cm}^{-2}$ , while for MOF and Pt/C+ $\text{RuO}_2$ , the corresponding values are 84  $\text{mW cm}^{-2}$  and 107  $\text{mW cm}^{-2}$ , respectively. The discharge voltage of  $\text{Fe}_{1.2}(\text{CoNi})_{1.8}\text{S}_6$  MES was around 1.07 V for more than 300 h at 5  $\text{mA cm}^{-2}$ , as displayed in Fig. 7d. The specific capacity of a battery based on  $\text{Fe}_{1.2}(\text{CoNi})_{1.8}\text{S}_6$  MES is as high as 808  $\text{mAh g}^{-1}$ , which is significantly larger than that of the MOF precursor (630  $\text{mAh g}^{-1}$ ) and Pt/C+ $\text{RuO}_2$  (589  $\text{mAh g}^{-1}$ ).

The continuous charge-discharge cycle test was carried out at 10  $\text{mA cm}^{-2}$  to further evaluate the long-term charge-discharge stability of liquid rechargeable Zn-air batteries. As shown in Fig. 7e,  $\text{Fe}_{1.2}(\text{CoNi})_{1.8}\text{S}_6$  MES can continuously and stably cycle for more than 140 h (about 420 cycles), while  $\text{Fe}_{1.2}(\text{CoNi})_{1.8}\text{-MOF}$  precursor and Pt/C+ $\text{RuO}_2$  can only stably cycle for less than 40 and 80 h. In order to better manifest the advantages of  $\text{Fe}_{1.2}(\text{CoNi})_{1.8}\text{S}_6$  MES in Zn-air batteries, the peak power density, specific capacity and cycling stability of  $\text{Fe}_{1.2}(\text{CoNi})_{1.8}\text{S}_6$  MES with reported catalysts were compared in Table S4. In the initial cycle, the charging voltage and discharging voltage of Zn-air battery based on  $\text{Fe}_{1.2}(\text{CoNi})_{1.8}\text{S}_6$  MES are 2.018 V and 1.059 V, respectively. The voltage difference of charging and discharging is 0.959 V and the round-trip efficiency is 52.5%. However, the corresponding data of Zn-air battery based on MOF precursor or Pt/C+ $\text{RuO}_2$  are (1.148 V, 42.7%) and (1.076 V, 45.4%), respectively (Table S5). The smaller charge-discharge voltage difference and higher efficiency indicated better battery performance. Small discharge voltages of Zn-air battery may be related to incomplete activation of battery performance at first. After 100 and 200 cycles, the voltage difference and round-trip efficiency of  $\text{Fe}_{1.2}(\text{CoNi})_{1.8}\text{S}_6$  MES were (0.924 V, 54.6) and (0.921 V, 54.7%),

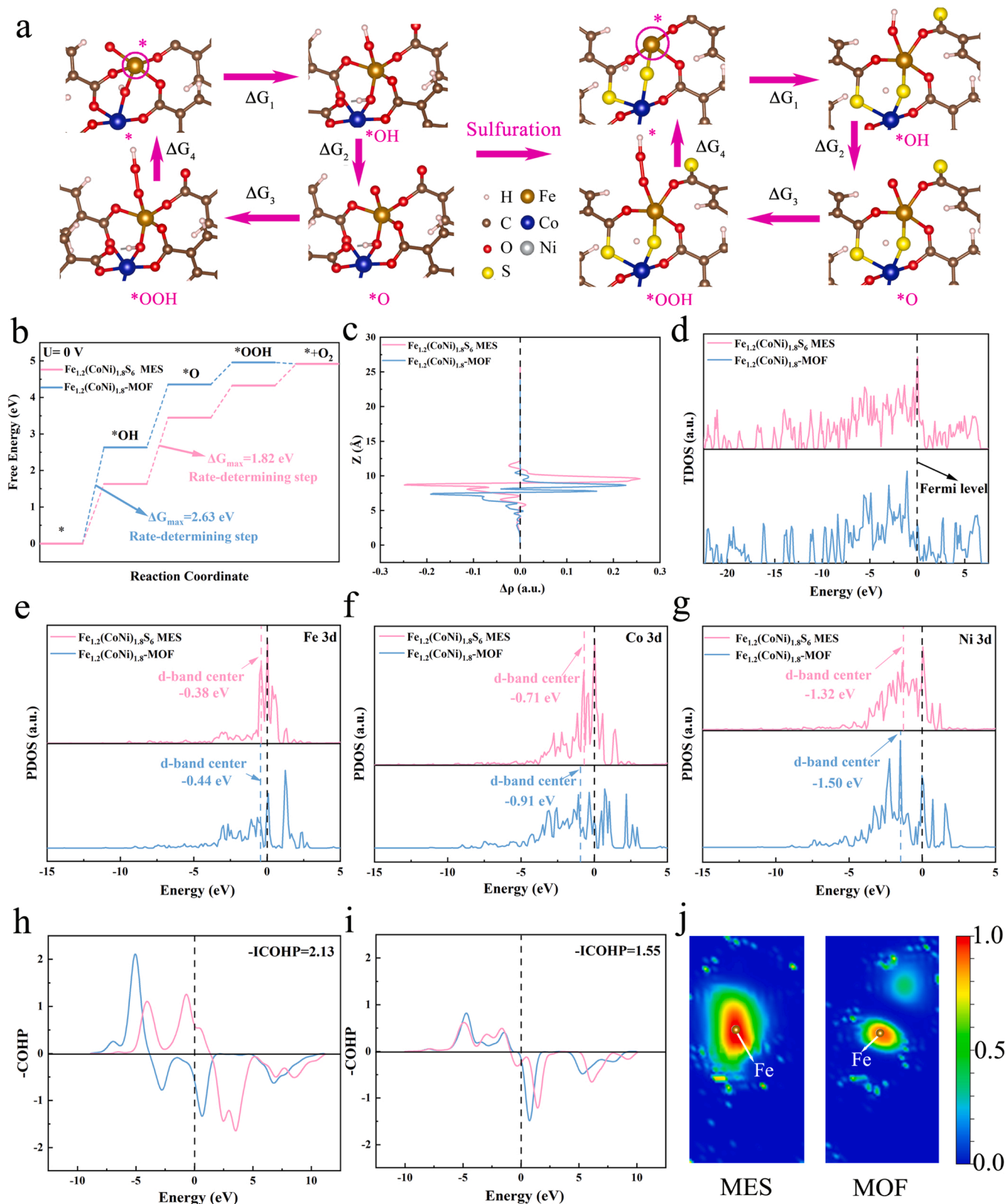


**Fig. 6.** (a) the OER steps on  $\text{Fe}_{1.2}(\text{CoNi})_{1.8}\text{-MOF}$  and  $\text{Fe}_{1.2}(\text{CoNi})_{1.8}\text{S}_6$  MES for DFT calculations, (b) Gibbs free energy diagram for the OER process in  $\text{Fe}_{1.2}(\text{CoNi})_{1.8}\text{-MOF}$  and  $\text{Fe}_{1.2}(\text{CoNi})_{1.8}\text{S}_6$  MES, (c) Plane-averaged charge density difference  $\Delta\rho(x)$  of  $\text{Fe}_{1.2}(\text{CoNi})_{1.8}\text{-MOF}$  and  $\text{Fe}_{1.2}(\text{CoNi})_{1.8}\text{S}_6$  MES along the z direction normal to the surface, (d) TDOS curves of  $\text{Fe}_{1.2}(\text{CoNi})_{1.8}\text{-MOF}$  and  $\text{Fe}_{1.2}(\text{CoNi})_{1.8}\text{S}_6$  MES. PDOS curves of  $\text{Fe}_{1.2}(\text{CoNi})_{1.8}\text{-MOF}$  and  $\text{Fe}_{1.2}(\text{CoNi})_{1.8}\text{S}_6$  MES, (e) Fe 3d, (f) Co 3d, (g) Ni 3d. Negative COHP curves of Fe-OH bond on the surface of (h)  $\text{Fe}_{1.2}(\text{CoNi})_{1.8}\text{S}_6$  MES, and (i)  $\text{Fe}_{1.2}(\text{CoNi})_{1.8}\text{-MOF}$ . (j) The side view of the ELF diagram of  $\text{Fe}_{1.2}(\text{CoNi})_{1.8}\text{S}_6$  MES and  $\text{Fe}_{1.2}(\text{CoNi})_{1.8}\text{-MOF}$ .



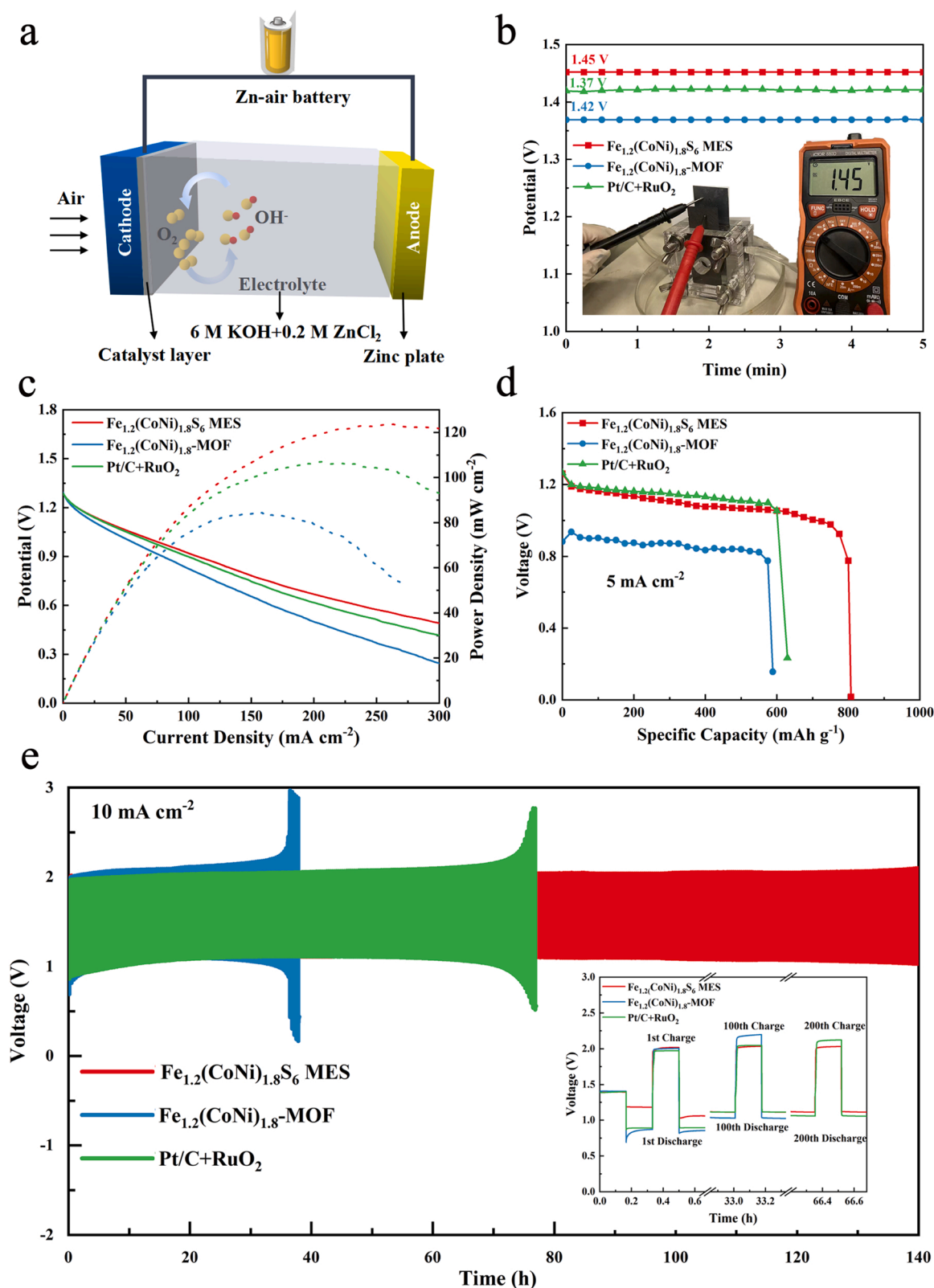


**Fig. 7.** (a) Schematic diagram of a Zn-air battery. (b) Open circuit potentials of Zn-air batteries. (c) Discharge polarization curves and the corresponding power density plots. (d) Voltage-capacity curves at  $5 \text{ mA cm}^{-2}$ . (e) Charge-discharge stability at a current density of  $10 \text{ mA cm}^{-2}$  (20 min for each cycle).

respectively, which is significantly better than MOF precursor and  $\text{Pt/C}$  (Table S6), indicating that Zn-air battery based on  $\text{Fe}_{1.2}(\text{CoNi})_{1.8}\text{S}_6$  MES exhibited best reversibility and stability. In conclusion, the  $\text{Fe}_{1.2}(\text{CoNi})_{1.8}\text{S}_6$  medium-entropy sulfide nanoparticles obtained by the two-step

method displays potential for application in rechargeable Zn-air batteries due to the excellent catalytic efficiency and stability of OER/ORR.

## 4. Conclusion

In this work, we developed a two-step method fabrication strategy to prepare  $\text{Fe}_{1.2}(\text{CoNi})_{1.8}\text{S}_6$  medium-entropy metal sulfides nanoparticles by  $\text{Fe}_{1.2}(\text{CoNi})_{1.8}$ -MOF precursor. The as-fabricated  $\text{Fe}_{1.2}(\text{CoNi})_{1.8}\text{S}_6$  medium-entropy metal sulfides nanoparticles exhibited significantly improved OER/ORR activity and stability compared to  $\text{Fe}_{1.2}(\text{CoNi})_{1.8}$ -MOF precursor. EELS and XPS showed that the valence states of active sites become higher significantly after sulfuration, which can further lower the limiting energy barrier to accelerate oxygen evolution reaction kinetics. Moreover, DFT calculations indicated that the electronic structure is regulated after the formation of medium-entropy metal sulfides nanoparticles. The electron transport resistance of  $\text{Fe}_{1.2}(\text{CoNi})_{1.8}\text{S}_6$  nanoparticles is lower than that of the precursor and thereby reducing the energy barrier of the rate-determining step via the stronger chemical bond during catalytic reaction process. The fabricated rechargeable zinc-air batteries display promising performance, including outstanding specific capacity, high power density and cyclic stability, which even surpass the commercial catalyst ( $\text{Pt/C}+\text{RuO}_2$ ). This study opens up a new direction toward preparing all kinds of medium-entropy nanoparticles (oxides, sulfides, selenides and phosphides, etc.) for applications in various electrocatalysis and energy storage systems.

## CRediT authorship contribution statement

**Hao Wu:** Writing – original draft, Methodology, Conceptualization, Formal analysis, Investigation. **Zexu Li:** Software, Conceptualization, Formal analysis, Investigation. **Zhichao Wang:** Writing – original draft, Formal analysis, Investigation. **Yujie Ma:** Methodology, Formal analysis. **Sirui Huang:** Formal analysis, Validation. **Fan Ding:** Software, Formal analysis, Validation. **Fengqi Li:** Investigation, Data curation. **Qingxi Zhai:** Formal analysis, Validation. **Yilun Ren:** Formal analysis, Investigation. **Xiaowen Zheng:** Formal analysis, Validation. **Yurong Yang:** Software, Investigation. **Shaochun Tang:** Funding acquisition, Validation. **Yu Deng:** Conceptualization, Formal analysis, Investigation. **Xiangkang Meng:** Supervision, Writing – review & editing, Conceptualization, Funding acquisition, Validation, Project administration.

## Declaration of Competing Interest

The authors declare that they have no known competing financial interests or personal relationships that could have appeared to influence the work reported in this paper.

## Data Availability

Data will be made available on request.

## Acknowledgements

This work was jointly supported by the National Natural Science Foundation of China (No. 51771090), the Key Research and Development Program of Jiangsu Provincial Department of Science and Technology of China (BE2022605), and the Fundamental Research Funds for the Central Universities (14380163).

## Appendix A. Supporting information

Supplementary data associated with this article can be found in the online version at [doi:10.1016/j.apcatb.2022.122356](https://doi.org/10.1016/j.apcatb.2022.122356).

## References

- [1] N.V. Bôas, J.B.S. Junior, L.C. Varanda, S.A.S. Machado, M.L. Calegaro, Bismuth and cerium doped cryptomelane-type manganese dioxide nanorods as bifunctional catalysts for rechargeable alkaline metal-air batteries, *Appl. Catal. B Environ.* 258 (2019), 118014, <https://doi.org/10.1016/j.apcatb.2019.118014>.

- [2] S. Sarkar, A. Biswas, E.E. Siddharthan, R. Thapa, R.S. Dey, Strategic modulation of target-specific isolated Fe,Co single-atom active sites for oxygen electrocatalysis impacting high power Zn–air battery, *ACS Nano* 16 (2022) 7890–7903, <https://doi.org/10.1021/acsnano.2c00547>.
- [3] S. Ramakrishnan, D.B. Velusamy, S. Sengodan, G. Nagaraju, D.H. Kim, A.R. Kim, D. J. Yoo, Rational design of multifunctional electrocatalyst: An approach towards efficient overall water splitting and rechargeable flexible solid-state zinc-air battery, *Appl. Catal. B Environ.* 300 (2022), 120752, <https://doi.org/10.1016/j.apcatb.2021.120752>.
- [4] X.L. Ao, J.H. Shi, W.D. Yi, Y.J. Que, L.Z. Zhang, H.Y. Bai, Y.M. Zhu, J. Wan, S. Chen, M. Yang, L. Huang, M. Gu, H. Pan, B.M. Xu, Co single-atom anchored on  $\text{Co}_3\text{O}_4$  and nitrogen-doped active carbon toward bifunctional catalyst for zinc-air batteries, *Appl. Catal. B Environ.* 260 (2020), 118188, <https://doi.org/10.1016/j.apcatb.2019.118188>.
- [5] L.H. Li, H. Chen, E. He, L. Wang, T.T. Ye, J. Lu, Y.D. Jiao, J.C. Wang, R. Gao, H. S. Peng, Y. Zhang, High-energy-density magnesium-air battery based on dual-layer gel electrolyte, *Angew. Chem. Int. Ed.* 60 (2021) 15317–15322, <https://doi.org/10.1002/anie.202104536>.
- [6] K.L. Ao, J.H. Shi, X.Y. Zhang, W.A. Daoud, Tuning oxygen vacancies in spinel nanosheets for binder-free oxygen cathodes with superior catalytic activity in zinc-air batteries, *J. Power Sources* 521 (2022), 230918, <https://doi.org/10.1016/j.jpowsour.2021.230918>.
- [7] D.S. Yu, Y.C. Ma, F. Hu, C.C. Lin, L.L. Li, H.Y. Chen, X.P. Han, S.J. Peng, Dual-sites coordination engineering of single atom catalysts for flexible metal-air batteries, *Adv. Energy Mater.* 11 (2021), 2101242, <https://doi.org/10.1002/aenm.202101242>.
- [8] X. Jia, H.J. Kang, X.X. Yang, Y.L. Li, K. Cui, X.H. Wu, W. Qin, G. Wu, Amorphous Ni (III)-based sulfides as bifunctional water and urea oxidation anode electrocatalysts for hydrogen generation from urea-containing water, *Appl. Catal. B* 312 (2022), 121389, <https://doi.org/10.1016/j.apcatb.2022.121389>.
- [9] J. Huang, H. Sheng, R.D. Ross, J. Han, X. Wang, B. Song, S. Jin, Modifying redox properties and local bonding of  $\text{Co}_3\text{O}_4$  by  $\text{CeO}_2$  enhances oxygen evolution catalysis in acid, *Nat. Commun.* 12 (2021) 3036, <https://doi.org/10.1038/s41467-021-23390-8>.
- [10] X.F. Lu, L.F. Gu, J.W. Wang, J.X. Wu, P.Q. Liao, G.R. Li, Bimetal-organic framework derived  $\text{CoFe}_2\text{O}_4/\text{C}$  porous hybrid nanorod arrays as high-performance electrocatalysts for Oxygen evolution reaction, *Adv. Mater.* 29 (2017), 1604437, <https://doi.org/10.1002/adma.201604437>.
- [11] R.J. Gao, J. Wang, Z.F. Huang, R.R. Zhang, W. Wang, L. Pan, J.F. Zhang, W.K. Zhu, X.W. Zhang, C.X. Shi, J.W. Lim, J.J. Zou, Pt/ $\text{Fe}_2\text{O}_3$  with Pt-Fe pair sites as a catalyst for oxygen reduction with ultralow Pt loading, *Nat. Energy* 6 (2021) 614–623, <https://doi.org/10.1038/s41560-021-00826-5>.
- [12] Z.F. Huang, J. Song, Y. Du, S. Xi, S. Dou, J.M.V. Nsanzimana, C. Wang, Z.J. Xu, X. Wang, Chemical and structural origin of lattice oxygen oxidation in Co-Zn oxyhydroxide oxygen evolution electrocatalysts, *Nat. Energy* 4 (2019) 329–338, <https://doi.org/10.1038/s41560-019-0355-9>.
- [13] K. Sada, R. Gond, N. Bothra, S.K. Pati, P. Barpanda, Potassium cobalt pyrophosphate as a nonprecious bifunctional electrocatalyst for zinc-air batteries, *ACS Appl. Mater. Interfaces* 14 (2022) 8992–9001, <https://doi.org/10.1021/acsaami.1c21481>.
- [14] S.Y. Lee, I.S. Kim, H.S. Cho, C.H. Kim, Y.K. Lee, Resolving potential-dependent degradation of electrodeposited  $\text{Ni}(\text{OH})_2$  catalysts in alkaline oxygen evolution reaction (OER): in situ XANES studies, *Appl. Catal. B* 284 (2021), 119729, <https://doi.org/10.1016/j.apcatb.2020.119729>.
- [15] X.X. Zou, Y. Zhang, Noble metal-free hydrogen evolution catalysts for water splitting, *Chem. Soc. Rev.* 44 (2015) 5148–5180, <https://doi.org/10.1039/C4CS00448E>.
- [16] S.S. Zheng, X.R. Li, B.Y. Yan, Q. Hu, Y.X. Xu, X. Xiao, H.G. Xue, H. Pang, Transition-metal (Fe, Co, Ni) based metal-organic frameworks for electrochemical energy storage, *Adv. Energy Mater.* 7 (2017), 1602733, <https://doi.org/10.1002/aenm.201602733>.
- [17] K.X. Song, Y. Feng, X.Y. Zhou, T.T. Qin, X. Zou, Y.G. Qi, Z.J. Chen, J.C. Rao, Z. Z. Wang, N.L. Yue, X. Ge, W. Zhang, W.T. Zheng, Exploiting the trade-offs of electron transfer in MOF-derived single Zn/Co atomic couples for performance-enhanced zinc-air battery, *Appl. Catal. B* 316 (2022), 121591, <https://doi.org/10.1016/j.apcatb.2022.121591>.
- [18] C.X. Zhao, J.N. Liu, J. Wang, C.D. Wang, X. Guo, X.Y. Li, X. Chen, L. Song, B.Q. Li, Q. Zhang, A clicking confinement strategy to fabricate transition metal single-atom sites for bifunctional oxygen electrocatalysis, *eabn5091*, *Sci. Adv.* 8 (2022), <https://doi.org/10.1126/sciadv.abn5091>.
- [19] Y. Feng, K.X. Song, W. Zhang, X.Y. Zhou, S.J. Yoo, J.G. Kim, S.F. Qiao, Y.G. Qi, X. Zou, Z.J. Chen, T.T. Qin, N.L. Yue, Z.Z. Wang, D.B. Li, W.T. Zheng, Efficient ORR catalysts for zinc-air battery: Biomass-derived ultra-stable Co nanoparticles wrapped with graphitic layers via optimizing electron transfer, *J. Energy Chem.* 70 (2022) 211–218, <https://doi.org/10.1016/j.jechem.2022.01.047>.
- [20] S.Y. Lin, L.X. Xia, L. Zhang, J.J. Feng, Y. Zhao, A.J. Wang, Highly active Fe centered FeM-N-doped carbon (M = Co/Ni/Mn): A general strategy for efficient oxygen conversion in Zn-air battery, *Chem. Eng. J.* 424 (2021), 130559, <https://doi.org/10.1016/j.cej.2021.130559>.
- [21] J.Y. Zhang, X.W. Bai, T.T. Wang, W. Xiao, P.X. Xi, J.L. Wang, D.Q. Gao, J. Wang, Bimetallic nickel cobalt sulfide as efficient electrocatalyst for Zn-air battery and water splitting, *Nano Micro Lett.* 11 (2019) 2, <https://doi.org/10.1007/s40820-018-0232-2>.
- [22] C. Li, Y.T. Gao, X.F. Xia, J.W. Zhu, X. Wang, Y.S. Fu, Hierarchically structured two-dimensional bimetallic CoNi-hexaaminobenzene coordination polymers derived

- from  $\text{Co(OH)}_2$  for enhanced oxygen evolution catalysis, *Small* 16 (2020), 1907043, <https://doi.org/10.1002/sml.201907043>.
- [23] D.Y. Xie, D.S. Yu, Y.N. Hao, S.L. Han, G.H. Li, X.L. Wu, F. Hu, L.L. Li, H.Y. Chen, Y. F. Liao, S.J. Peng, Dual-active sites engineering of N-doped hollow carbon nanocubes confining bimetal alloys as bifunctional oxygen electrocatalysts for flexible metal-air batteries, *Small* 17 (2021), 2007239, <https://doi.org/10.1002/sml.202007239>.
- [24] Y.F. Kao, S.K. Chen, T.J. Chen, P.C. Chu, J.W. Yeh, S.J. Lin, Electrical, magnetic, and Hall properties of  $\text{Al}_x\text{CoCrFeNi}$  high-entropy alloys, *J. Alloy. Compd.* 509 (2011) 1607–1614, <https://doi.org/10.1016/j.jallcom.2010.10.210>.
- [25] M. Bondesgaard, N.L.N. Broge, A. Mamakhel, M. Bremholm, B.B. Iversen, General solvothermal synthesis method for complete solubility range bimetallic and high-entropy alloy nanocatalysts, *Adv. Funct. Mater.* 29 (2019), 1905933, <https://doi.org/10.1002/adfm.201905933>.
- [26] M.J. Cui, C.P. Yang, B.Y. Li, Q. Dong, M.L. Wu, S. Hwang, H. Xie, X.Z. Wang, G. F. Wang, L.B. Hu, High-entropy metal sulfide nanoparticles promise high-performance oxygen evolution reaction, *Adv. Energy Mater.* 11 (2021), 2002887, <https://doi.org/10.1002/aenm.202002887>.
- [27] T.X. Nguyen, Y.H. Su, C.C. Lin, J.J. Ruan, J.M. Ting, A new high entropy glycerate for high performance oxygen evolution reaction, *Adv. Sci.* 8 (2021), 2002446, <https://doi.org/10.1002/advs.202002446>.
- [28] Z.J. Chen, T. Zhang, X.Y. Gao, Y.J. Huang, X.H. Qin, Y.F. Wang, K. Zhao, X. Peng, C. Zhang, L. Liu, M.H. Zeng, H.B. Yu, Engineering microdomains of oxides in high-entropy alloy electrodes toward efficient oxygen evolution, *Adv. Mater.* 33 (2021), 2101845, <https://doi.org/10.1002/adma.202101845>.
- [29] X.Y. Li, K. Lu, Playing with defects in metals, *Nat. Mater.* 16 (2017) 700–701, <https://doi.org/10.1038/nmat4929>.
- [30] X.Y. Li, K. Lu, Improving sustainability with simpler alloys, *Science* 364 (2019) 733–734, <https://doi.org/10.1126/science.aaw9905>.
- [31] S.Z. Zhi, J.B. Li, L.P. Hu, J.Q. Li, N. Li, H.J. Wu, F.S. Liu, C.H. Zhang, W.Q. Ao, H. P. Xie, X.B. Zhao, S.J. Pennycook, T.J. Zhu, Medium entropy-enabled high performance cubic  $\text{GeTe}$  thermoelectrics, *Adv. Sci.* 8 (2021), 2100220, <https://doi.org/10.1002/advs.202100220>.
- [32] H. Park, J. Wung Bae, T.H. Lee, I.J. Park, C. Kim, M.G. Lee, S.A. Lee, J.W. Yang, M. J. Choi, S.H. Hong, S.Y. Kim, S.H. Ahn, J.Y. Kim, H.S. Kim, H.W. Jang Surface-tailored, medium entropy alloys as radically low overpotential oxygen evolution electrocatalysts, *Small* 18 (2022), 2105611, <https://doi.org/10.1002/sml.202105611>.
- [33] F.D.C.G. Filho, R.O. Ritchie, M.A. Meyers, S.N. Monteiro, Cantor-derived medium-entropy alloys: bridging the gap between traditional metallic and high entropy alloys, *J. Mater. Res. Technol.* 17 (2022) 1868–1895, <https://doi.org/10.1016/j.jmrt.2022.01.118>.
- [34] Y.G. Yao, Z.N. Huang, P.F. Xie, S.D. Lacey, R.J. Jacob, H. Xie, F.J. Chen, A.M. Nie, T.C. Pu, M. Rehboldt, D.W. Yu, M.R. Zachariah, C. Wang, R. Shahbazian-Yassar, J. Li, L.B. Hu, Carbothermal shock synthesis of high-entropy-alloy NPs, *Science* 359 (2018) 1489–1494, <https://doi.org/10.1126/science.aan5412>.
- [35] R.Q. Yao, Y.T. Zhou, H. Shi, W.B. Wan, Q.H. Zhang, L. Gu, Y.F. Zhu, Z. Wen, X. Y. Lang, Q. Jiang, Nanoporous surface high-entropy alloys as highly efficient multisite electrocatalysts for nonacidic hydrogen evolution reaction, *Adv. Funct. Mater.* 31 (2021), 2009613, <https://doi.org/10.1002/adfm.202009613>.
- [36] Y.W. Li, T. Zhao, M.T. Lu, Y.H. Wu, Y.B. Xie, H. Xu, J.K. Gao, J.M. Yao, G.D. Qian, Q.C. Zhang, Enhancing oxygen evolution reaction through modulating electronic structure of trimetallic electrocatalysts derived from metal-organic frameworks, *Small* 15 (2019), 1901940, <https://doi.org/10.1002/sml.201901940>.
- [37] S.Q. Wang, W.Y. Huo, F. Fang, Z.H. Xie, J.K. Shang, J.Q. Jiang, High entropy alloy/C nanoparticles derived from polymeric MOF as promising electrocatalysts for alkaline oxygen evolution reaction, *Chem. Eng. J.* 429 (2022), 132410, <https://doi.org/10.1016/j.cej.2021.132410>.
- [38] B.K. Kang, S.Y. Im, J. Lee, S.H. Kwag, S.B. Kwon, S. Tiruneh, M.J. Kim, J.H. Kim, W.S. Yang, B. Lim, D.H. Yoon, In-situ formation of MOF derived mesoporous  $\text{Co}_3\text{N}$ /amorphous N-doped carbon nanocubes as an efficient electrocatalytic oxygen evolution reaction, *Nano Res* 12 (2019) 1605–1611, <https://doi.org/10.1007/s12274-019-2399-3>.
- [39] X.F. Lu, Y.J. Fang, D.Y. Luan, X.W. Lou, Metal-organic frameworks derived functional materials for electrochemical energy storage and conversion: A mini review, *Nano Lett.* 21 (2021) 1555–1565, <https://doi.org/10.1021/acs.nanolett.0c04898>.
- [40] Z.H. Zou, T.T. Wang, X.H. Zhao, W.J. Jiang, H.R. Pan, D.Q. Gao, C.L. Xu, Expediting in-situ electrochemical activation of two-dimensional metal-organic frameworks for enhanced OER intrinsic activity by iron incorporation, *ACS Catal.* 9 (2019) 7356–7364, <https://doi.org/10.1021/acscatal.9b00072>.
- [41] G. Kresse, J. Hafner, Ab-initio molecular-dynamics simulation of the liquid-metal amorphous-semiconductor transition in germanium, *Phys. Rev. B* 49 (1994) 14251–14269, <https://doi.org/10.1103/PhysRevB.49.14251>.
- [42] G. Kresse, J. Furthmüller, Efficiency of ab-initio total energy calculations for metals and semiconductors using a plane-wave basis set - Science Direct, *Comput. Mater. Sci.* 6 (1996) 15–50, [https://doi.org/10.1016/0927-0256\(96\)00008-0](https://doi.org/10.1016/0927-0256(96)00008-0).
- [43] J.P. Perdew, K. Burke, M. Ernzerhof, Generalized gradient approximation made simple, *Phys. Rev. Lett.* 77 (1996) 3865, <https://doi.org/10.1103/PhysRevLett.77.3865>.
- [44] G.T. Hai, X.L. Jia, K.Y. Zhang, X. Liu, Z.Y. Wu, G. Wang, High-performance oxygen evolution catalyst using two-dimensional ultrathin metal-organic frameworks nanosheets, *Nano Energy* 44 (2018) 345–352, <https://doi.org/10.1016/j.nanoen.2017.11.071>.
- [45] X.P. Han, G.W. He, Y. He, J.F. Zhang, X.R. Zheng, L.L. Li, C. Zhong, W.B. Hu, Y. D. Deng, T.Y. Ma, Engineering catalytic active sites on cobalt oxide surface for enhanced oxygen electrocatalysis, *Adv. Energy Mater.* 8 (2018), 1702222, <https://doi.org/10.1002/aenm.201702222>.
- [46] X. Zhang, F. Yan, X.Z. Ma, C.L. Zhu, Y. Wang, Y. Xie, S.L. Chou, Y.J. Huang, Y. J. Chen, Regulation of morphology and electronic structure of  $\text{FeCoNi}$  layered double hydroxides for highly active and stable water oxidation catalysts, *Adv. Energy Mater.* 11 (2021), 2102141, <https://doi.org/10.1002/aenm.202102141>.
- [47] X. Wang, X.K. Huang, W.B. Gao, Y. Tang, P.B. Jiang, K. Lan, R.Z. Yang, B. Wang, R. Li, Metal-organic framework derived  $\text{CoTe}_2$  encapsulated in nitrogen-doped carbon nanotube frameworks: a high-efficiency bifunctional electrocatalyst for overall water splitting, *J. Mater. Chem. A* 6 (2018) 3684–3691, <https://doi.org/10.1039/C7TA10728E>.
- [48] Y. Gao, H. Li, G. Yang, Amorphous nickel hydroxide nanosheets with ultrahigh activity and super-long-term cycle stability as advanced water oxidation catalysts, *Cryst. Growth Des.* 15 (2015) 4475–4483, <https://doi.org/10.1021/acs.cgd.5b00752>.
- [49] Z. Jia, T. Yang, L.G. Sun, Y.L. Zhao, W.P. Li, J.H. Luan, F.C. Lyu, L. Zhang, J. J. Kruzic, J. Kai, J.C. Huang, J. Lu, C.T. Liu, A novel multinary intermetallic as an active electrocatalyst for hydrogen evolution, *Adv. Mater.* 32 (2020), 2000385, <https://doi.org/10.1002/adma.202000385>.
- [50] C.L. Hu, L. Zhang, Z.J. Zhao, A. Li, X.X. Chang, J.L. Gong, Synergism of geometric construction and electronic regulation: 3D  $\text{Se}(\text{NiCo})\text{S}_x/(\text{OH})_x$  nanosheets for highly efficient overall water splitting, *Adv. Mater.* 30 (2018), 1705538, <https://doi.org/10.1002/adma.201705538>.
- [51] H. Li, Y. Han, H. Zhao, W. Qi, D. Zhang, Y. Yu, W.W. Cai, S.X. Li, J.P. Lai, B. L. Huang, L. Wang, Fast site-to-site electron transfer of high-entropy alloy nanocatalyst driving redox electrocatalysis, *Nat. Commun.* 11 (2020) 5437, <https://doi.org/10.1038/s41467-020-19277-9>.
- [52] Y.P. Wang, B.S. Li, H.Z. Fu, Solid solution or intermetallics in a high-entropy alloy, *Adv. Eng. Mater.* 11 (2009) 641–644, <https://doi.org/10.1002/adem.200900057>.
- [53] L. Cavé, T. Al, D. Loomer, S. Cogswell, L. Weaver, A STEM/EELS method for mapping iron valence ratios in oxide minerals, *Micron* 37 (2006) 301–309, <https://doi.org/10.1016/j.micron.2005.10.006>.
- [54] Z.Y. Wang, D. Santhanagopalan, W. Zhang, F. Wang, H.L.L. Xin, K. He, J.C. Li, N. Dudney, Y.S. Meng, In situ STEM-EELS observation of nanoscale interfacial phenomena in all-solid-state batteries, *Nano Lett.* 16 (2016) 3760–3767, <https://doi.org/10.1021/acs.nanolett.6b01119>.
- [55] N. Zhang, X.B. Feng, D.W. Rao, X. Deng, L.J. Cai, B.C. Qiu, R. Long, Y.J. Xiong, Y. Lu, Y. Chai, Lattice oxygen activation enabled by high-valence metal sites for enhanced water oxidation, *Nat. Commun.* 11 (2020) 4066, <https://doi.org/10.1038/s41467-020-17934-7>.
- [56] M. Liu, Y.J. Ji, Y.Y. Li, P.F. An, J. Zhang, J.Q. Yan, S.Z. Liu, Single-atom doping and high-valence state for synergistic enhancement of NiO electrocatalytic water oxidation, *Small* 17 (2021), 2102448, <https://doi.org/10.1002/sml.202102448>.
- [57] T.X. Nguyen, Y.C. Liao, C.C. Lin, Y.H. Su, J.M. Ting, Advanced high entropy perovskite oxide electrocatalyst for oxygen evolution reaction, *Adv. Funct. Mater.* 31 (2021), 2101632, <https://doi.org/10.1002/adfm.202101632>.
- [58] N. Li, T. Meng, L. Ma, H. Zhang, J.J. Yao, M.W. Xu, C.M. Li, J. Jiang, Curtailing carbon usage with addition of functionalized  $\text{NiFe}_2\text{O}_4$  quantum dots: toward more practical S cathodes for Li-S cells, *Nano Micro Lett.* 12 (2020) 145, <https://doi.org/10.1007/s40820-020-00484-4>.
- [59] S. Anantharaj, S. Kundu, S. Noda, The Fe Effect: A review unveiling the critical roles of Fe in enhancing oer activity of Ni and Co based catalysts, *Nano Energy* 80 (2021), 105514, <https://doi.org/10.1016/j.nanoen.2020.105514>.
- [60] W. Liu, E. Hu, H. Jiang, Y. Xiang, Z. Weng, M. Li, Q. Fan, X.Q. Yu, E.I. Altman, H. L. Wang, A highly active and stable hydrogen evolution catalyst based on pyrite-structured cobalt phosphosulfide, *Nat. Commun.* 7 (2016) 10771, <https://doi.org/10.1038/ncomms10771>.
- [61] H. Chen, L.F. Hu, M. Chen, Y. Yan, L.M. Wu, Nickel-cobalt layered double hydroxide nanosheets for high-performance supercapacitor electrode materials, *Adv. Funct. Mater.* 24 (2014) 934–942, <https://doi.org/10.1002/adfm.201301747>.
- [62] F.L. Li, P.T. Wang, X.Q. Huang, D.J. Young, H.F. Wang, P. Braunstein, J.P. Lang, Large-scalable, bottom-up synthesis of binary metal-organic framework nanosheets for efficient water oxidation, *Angew. Chem. Int. Ed.* 58 (2019) 7051–7056, <https://doi.org/10.1002/anie.201902588>.
- [63] D.J. Zhou, Z. Cai, X.D. Lei, W.L. Tian, Y.M. Bi, Y. Jia, N.N. Han, T.F. Gao, Q. Zhang, Y. Kuang, J.Q. Pan, X.M. Sun, X. Duan, NiCoFe-layered double hydroxides/N-doped graphene oxide array colloid composite as an efficient bifunctional catalyst for oxygen electrocatalytic reactions, *Adv. Energy Mater.* 8 (2018), 1701905, <https://doi.org/10.1002/aenm.201701905>.
- [64] H.V.D. Heide, R. Hemmel, C.F.V. Bruggen, C. Haas, X-ray photoelectron spectra of 3d transition metal pyrites, *J. Solid State Chem.* 33 (1980) 17–25, [https://doi.org/10.1016/0022-4596\(80\)90543-5](https://doi.org/10.1016/0022-4596(80)90543-5).
- [65] H. Tian, L.M. Zeng, Y.F. Huang, Z.H. Ma, G. Meng, L.X. Peng, C. Chen, X.Z. Cui, J. L. Shi, In situ electrochemical Mn(III)/Mn(IV) generation of Mn(II)O electrocatalysts for high-performance oxygen reduction, *Nano-Micro Lett.* 12 (2020) 161, <https://doi.org/10.1007/s40820-020-00500-7>.
- [66] X.F. Lu, Y. Chen, S.B. Wang, S.Y. Gao, X.W. Lou, Interfacing manganese oxide and cobalt in porous graphitic carbon polyhedrons boosts oxygen electrocatalysis for Zn-Air batteries, *Adv. Mater.* 31 (2019), 1902339, <https://doi.org/10.1002/adma.201902339>.
- [67] X.F. Lu, S.L. Zhang, E.B. Shangguan, P. Zhang, S.Y. Gao, X.W. Lou, Nitrogen-doped cobalt pyrite yolk-shell hollow spheres for long-life rechargeable Zn-Air batteries, *Adv. Sci.* 7 (2020), 2001178, <https://doi.org/10.1002/advs.202001178>.
- [68] T.X. Nguyen, Y.H. Su, C.C. Lin, J.M. Ting, Self-reconstruction of sulfate-containing high entropy sulfide for exceptionally high-performance oxygen evolution reaction



- electrocatalyst, *Adv. Funct. Mater.* 31 (2021), 2106229, <https://doi.org/10.1002/adfm.202106229>.
- [69] H. Su, S.J. Song, S.S. Li, Y.Q. Gao, L. Ge, W.Y. Song, T.Y. Ma, J. Liu, High-valent bimetal  $\text{Ni}_3\text{S}_2/\text{Co}_3\text{S}_4$  induced by Cu doping for bifunctional electrocatalytic water splitting, *Appl. Catal. B* 293 (2021), 120225, <https://doi.org/10.1016/j.apcatb.2021.120225>.
- [70] S. Zhang, B.L. Huang, L.G. Wang, X.Y. Zhang, H.S. Zhu, X.Q. Zhu, J. Li, S.J. Guo, E. K. Wang, Boosted oxygen evolution reactivity via atomic iron doping in cobalt carbonate hydroxide hydrate, *ACS Appl. Mater. Interfaces* 12 (2020) 40220–40228, <https://doi.org/10.1021/acsami.0c07260>.
- [71] L.J. Zhang, W.W. Cai, N.Z. Bao, Top-level design strategy to construct an advanced high-entropy Co-Cu-Fe-Mo (oxy)hydroxide electrocatalyst for the oxygen evolution reaction, *Adv. Mater.* 33 (2021), 2100745, <https://doi.org/10.1002/adma.202100745>.
- [72] L. Zhang, Z.J. Shao, X.M. Cao, P. Hu, Insights into different products of nitrosobenzene and nitrobenzene hydrogenation on Pd (111) under realistic reaction conditions, *J. Phys. Chem. C* 122 (2018) 20337–20350, <https://doi.org/10.1021/acs.jpcc.8b05364>.
- [73] X. Huang, X. Xu, C. Li, D. Wu, D. Cheng, D. Cao, Vertical CoP nanoarray wrapped by N, P-doped carbon for hydrogen evolution reaction in both acidic and alkaline conditions, *Adv. Energy Mater.* 9 (2019), 1803970, <https://doi.org/10.1002/aenm.201803970>.